Geophysical Journal International

Geophys. J. Int. (2023) **234,** 771–789 https://doi.org/10.1093/gji/ggad096
Advance Access publication 2023 March 03
GJI Applied and marine geophysics

Surface waves at a fluid/double-porosity medium interface

Enjiang Wang,[1,2] José M. Carcione[3,4] and Jing Ba[3]

[1] *Key Lab of Submarine Geosciences and Prospecting Techniques, MOE, College of Marine Geosciences, Ocean University of China, Qingdao,* 266100*, China*
[2] *Frontiers Science Center for Deep Ocean Multispheres and Earth System, Qingdao* 266100*, China*
[3] *School of Earth Sciences and Engineering, Hohai University, Nanjing* 211100*, China. E-mail: jba@hhu.edu.cn*
[4] *National Institute of Oceanography and Applied Geophysics - OGS, Trieste, Italy*

Accepted 2023 March 2. Received 2023 February 27; in original form 2022 June 29

SUMMARY

We consider surface-wave propagations at an interface separating a fluid layer and a double-porosity medium embedded with cracks. The theory is based on a generalization of the Biot-Rayleigh model from spherical cavities to penny-shaped cracks randomly embedded into a host medium, where mesoscopic local fluid flow (LFF) plays an important role. We derive closed-form dispersion equations of surface waves, based on potentials and suitable boundary conditions (BCs), to obtain the phase velocity and attenuation by using numerical iterations. Two special cases are considered by letting the thickness of the fluid (water) layer to be zero and infinity. We obtain pseudo-Rayleigh and pseudo-Stoneley waves for zero and infinite thickness and high-order surface modes for finite nonzero thickness. Numerical examples confirm that the LFF affects the propagation at low frequencies, causing strong attenuation, whereas the impact of BCs is mainly observed at high frequencies, due to the propagation of slow wave modes. The crack density mainly affects the level of attenuation, whereas the aspect ratio the location of the relaxation peak. The fundamental mode undergoes a significant velocity dispersion, whose location moves to low frequencies as the thickness increases. In all cases, there also exist two slower surface modes that resemble the two slow body waves, only present for sealed BCs.

Key words: Wave propagation; Surface waves and free oscillations; Interface waves; Seismic attenuation; Computational seismology.

1 INTRODUCTION

Propagation of surface and interface waves in porous media finds applications in a variety of fields, such as geotechnical engineering, seismology, borehole logging and exploration geophysics (Norris 1989; Tang & Cheng 1996; Yang 2005; Markov 2009; Zhang & Müller 2019). Specifically, a quantitative investigation is important for mapping the spatial distribution of medium properties, such as permeability, porosity and saturation, which are essential for reservoir characterization and fluid identification (Tang & Cheng 1996).

Many theories have been developed to describe wave motion in porous media. Biot (1956, 1962) pioneered the study, and formulated a set of equations for phenomenological wave propagation in a medium saturated by a single fluid. The theory predicts two compressional waves (P1 and P2) and one shear wave (S). The second compressional wave is diffusive at low frequencies and wave-like at high frequencies. The related surface waves, generated from the interference among the three body waves, can be quite different from the classic ones of the elastic case. Considering the free surface of a porous half-space, Deresiewicz (1962) showed the existence of a Rayleigh-type wave, and analyzed the frequency-dependent phase velocity and dissipation. Tajuddin (1984) examined the effects of permeable and impermeable boundaries on Rayleigh-wave propagation. Zhang *et al.* (2011) further discussed the influence of partially permeable boundaries, and reported two Rayleigh waves, where the second one propagates slightly slower than the bulk slow P2 wave, but exists only for impermeable and partially permeable conditions.

On the other hand, other studies focus on the surface-wave propagations at a liquid/poroelastic flat interface (Feng & Johnson 1983; Gubaidullin *et al.* 2004; Chao *et al.* 2006; van Dalen *et al.* 2011). Deresiewicz (1964) derived the dispersion equations for Stoneley-wave propagation in a porous half-space lying under a liquid layer, and further obtained asymptotic expressions at low frequencies. Feng & Johnson (1983) investigated surface-wave propagations at high frequencies at an interface between a fluid and a fluid-saturated half space. Their results confirm the existence of three interface waves, namely, the pseudo-Rayleigh wave, the pseudo-Stoneley wave and the true interface wave, depending on the BCs at the interface. The true surface wave propagates slower than the body waves in both the fluid and porous medium, and exists only for sealed-pore boundaries. The pseudo-Rayleigh wave propagates faster than the bulk mode in the fluid and the slow mode, but slower than the P1 and SV waves in the porous medium. The pseudo-Stoneley wave has a velocity higher than that of the slow P2 wave. Hence, the so-called pseudo interface wave leaks part of its energy into slower bulk modes as it propagates along the interface. The results are confirmed experimentally by high-frequency sonic measurements (Mayes *et al.* 1986; Adler & Nagy 1994), and numerically by a novel algorithm based on the Fourier and Chebyshev pseudospectral methods (Sidler *et al.* 2010). With the same configuration, Gubaidullin *et al.* (2004) incorporated the influence of a frequency-dependent viscous correction factor. Chao *et al.* (2006) studied the effect of partially saturated gas bubbles on velocity and attenuation of surface wave modes, using a modified Biot theory. Markov (2009) considered the interface between two fluid-saturated porous media, and studied the frequency-dependent velocity and attenuation of the Stoneley surface wave. More recently, Qiu *et al.* (2019) considered a liquid/porous-medium interface underlaid by a hard porous half-space, and analyzed the propagation of pseudo-Rayleigh and pseudo-Scholte waves.

In many cases, the Biot theory is insufficient in estimating the broadband velocity dispersion and attenuation. Squirt-flow mechanisms have been introduced to explain attenuation at ultrasonic frequencies (Dvorkin & Nur 1993; Dvorkin *et al.* 1995; Carcione & Gurevich 2011). It occurs mainly at the microscopic pore scale, due to the different compliances of the soft and stiff pores. Using the theory of Dvorkin *et al.* (1995), Sharma (2018) analyzed the effect of squirt flow on the propagation of Rayleigh waves, including phase velocity, attenuation and polarisation. Alternatively, mesoscopic flow has been introduced to account for attenuation at seismic frequencies (Pride *et al.* 2004; Müller *et al.* 2010; Carcione 2022). It occurs due to the heterogeneities at a scale much larger than the pore size but smaller than the wavelength. Many theories are developed to explain this mechanism, among which, the double-porosity theory is a simple one. Pride & Berryman (2003a, 2003b) considered a model containing both the storage and fracture porosities, and derived a frequency-dependent compressibility law to describe the fluid transfer between these pore spaces, which predicts realistic attenuation at the exploration-geophysics band. It becomes an effective Biot model when the heterogeneity phase is embedded in the host phase (Pride *et al.* 2004). Based on this theory, Dai *et al.* (2006) analyzed Rayleigh-wave propagation in a double-porosity half-space with permeable boundaries, and discussed the effect of porosity and fracture permeability. In addition, Ba *et al.* (2011) proposed another double-porosity model based on Biot theory and the Rayleigh model of bubble oscillations. The theory is adopted by Sharma (2014) to study the effect of local fluid flow (LFF) on propagation and polarization of Rayleigh waves in a double-porosity half-space. His results suggest the existence of an additional (second) Rayleigh wave when the saturating fluid has a low viscosity. This second wave attenuates less and propagates much faster than the first Rayleigh wave.

Cracks play an important role in wave propagation, affecting the properties of the skeleton and the fluid flow. Specifically, significant LFF occurs between compliant cracks and relatively stiff pores, due to their dissimilar pore volumes, permeabilities and compressibilities (Carcione *et al.* 2010; Müller *et al.* 2010). To take these properties into account, Sharma (1996) introduced fluid-saturated cracks into a porous medium and established a modified Biot theory where the elastic constants and dynamical parameters are in accordance with the theory of Budiansky and O'Connell (1976). Then, he studied surface-wave propagation in a saturated poroelastic half-space lying under a uniform layer of liquid. Chapman *et al.* (2002) proposed a Gassmann-consistent squirt-flow model by considering a microstructure composed of randomly oriented thin cracks and spherical pores. Using the fluid-mass conservation and the T-matrix approach, Jakobsen & Chapman (2009) established a crack-porous model that unifies the global and squirt flows. Tang *et al.* (2012) incorporated randomly oriented cracks into Biot's theory, and proposed a pore-crack model, where squirt flow is taken into account. One advantage of this theory is that, the relaxation parameter is no longer necessary, because it can be expressed by the crack density and aspect ratio. Other models consider anisotropy induced by cracks (Galvin & Gurevich 2009; Fu *et al.* 2018; Guo & Gurevich 2020). For example, Galvin & Gurevich (2009) considered a poroelastic medium with a distribution of aligned penny-shaped cracks and confirmed frequency-dependent anisotropy and attenuation using a multiple-scattering theory. Fu *et al.* (2018) developed an alternative solution by using the Waterman-Truell scattering approximation for a distribution of aligned silt cracks.

Zhang *et al.* (2019) established an extended Biot-Rayleigh double-porosity model, where the spherical inclusions were replaced by randomly-oriented penny-shaped cylindrical cracks, where LFF plays an important role. It is consistent with Gassmann equations and honors experimental data. The theory has been used to study the reflection of inhomogeneous waves at the free surface of a cracked porous medium (Kumari & Kumar 2022). Using this theory, the present work focuses on the propagation of surface and interface waves, and analyzes the effect of cracks and the associated LFF. A flat interface separating a double-porosity half-space and a fluid (water) layer of thickness H is considered. The corresponding surface-wave dispersion equations are derived in closed form, based on potentials under sealed or open BCs. By letting $H = 0$ and $H = +\infty$, two special cases are obtained, corresponding to the propagations of pseudo-Rayleigh and pseudo-Stoneley waves, respectively. The phase velocity and attenuation factor, as a function of frequency and obtained from an iterative method, are illustrated, and the effects of LFF, BCs, crack density and aspect ratio and water thickness H are discussed.

2 GOVERNING DIFFERENTIAL EQUATIONS

The crack-double-porosity theory of Zhang *et al.* (2019) involves two porosities, namely a local porosity ϕ_{10} of the host medium with a large volume fraction f_1, and a local porosity ϕ_{20} of the inclusions (cracks) with a smaller volume fraction $f_2 = 1 - f_1$. The two porosities are associated to different permeabilities and compressibilities, which therefore induce pressure gradients when the wave propagates, and consequently relative fluid flows. The inclusions (cracks) are assumed to be penny-shaped and cylindrical with the radius R_0 and height h being much smaller than the wavelength, which correspond to a mesoscopic-scale length (Zhang *et al.* 2019).

With $\mathbf{u}$, $\mathbf{U}^{(1)}$ and $\mathbf{U}^{(2)}$ denoting the averaged displacement vectors of the matrix, fluid in host medium, and fluid in cracks, respectively, the strain-displacement relations are

$$\epsilon_{ij} = \frac{1}{2}(\partial_i u_j + \partial_j u_i),\ \epsilon = \nabla \cdot \mathbf{u},\ \eta^{(m)} = \nabla \cdot \mathbf{U}^{(m)},\ m = 1, 2 \quad (1)$$

where, ϵ_{ij} are the solid strain components, ϵ and $\eta^{(m)}$ are the averaged volumetric strains of the solid and the two variations of fluid content in the host ($m = 1$) and inclusions ($m = 2$), respectively.

Let σ_{ij} and σ_m be the solid stress components and fluid stresses in the two phases, and ς the fluid variation between the host medium and the penny-shaped cracks. We have

$$
\begin{aligned}
\sigma_1 &= Q_1\epsilon + R_1(\eta^{(1)} + \phi_2\varsigma),\\
\sigma_2 &= Q_2\epsilon + R_2(\eta^{(2)} - \phi_1\varsigma),\\
\sigma_{ij} &= 2N\epsilon_{ij} + \left[A\epsilon + Q_1(\eta^{(1)} + \phi_2\varsigma) + Q_2(\eta^{(2)} - \phi_1\varsigma)\right]\delta_{ij}, \quad (2)
\end{aligned}
$$

where δ_{ij} is the Kronecker delta, $\phi_m = f_m\phi_{m0}$ are the porosities of the host medium and inclusions, A and N are the composite moduli equivalent to the Lamé constants in the theory of elasticity (Biot 1962), Q_m represent the coupling between the volume change of the solid and that of the fluid, and R_m are the pressures required on the fluid to inject a given volume of fluid into the aggregate whereas the total volume remains constant. These quantities are given in Appendix A.

The equation of motion for the mesoscopic fluid-flow variable ς is derived by a generalization of the Biot-Rayleigh theory (Ba *et al.* 2011) from spherical inclusions to penny-shaped cracks, where the microvelocity fields inside the inclusions are additionally considered. It is

$$
\begin{aligned}
&\left(\frac{3}{8} + \frac{\phi_{20}}{2\phi_{10}}\ln\frac{L+R_0}{R_0}\right)\phi_1^2\phi_2\rho_f R_0^2\ddot{\varsigma}\\
&\quad + \left(\frac{3\eta}{8\kappa_2} + \frac{\eta}{2\kappa_1}\ln\frac{L+R_0}{R_0}\right)\phi_{20}\phi_1^2\phi_2 R_0^2\dot{\varsigma}\\
&= \left[\phi_2 Q_1 - \phi_1 Q_2\right]\epsilon + \phi_2 R_1\eta^{(1)} - \phi_1 R_2\eta^{(2)}\\
&\quad + (\phi_2^2 R_1 + \phi_1^2 R_2)\varsigma, \qquad (3)
\end{aligned}
$$

where an overdot denotes the time derivative, ρ_f is the fluid density, η is the fluid viscosity, κ_1 and κ_2 are the permeabilities of the host medium and inclusions, respectively, and $L = (R_0^2/12)^{1/2}$ is the characteristic fluid flow length.

The equations of momentum conservation are

$$
\begin{aligned}
\sigma_{ij,j} &= \rho_{00}\ddot{u}_i + \rho_{01}\ddot{U}_i^{(1)} + \rho_{02}\ddot{U}_i^{(2)} + b_1(\dot{u}_i - \dot{U}_i^{(1)})\\
&\quad + b_2(\dot{u}_i - \dot{U}_i^{(2)}),\\
(\sigma_1)_{,i} &= \rho_{01}\ddot{u}_i + \rho_{11}\ddot{U}_i^{(1)} - b_1(\dot{u}_i - \dot{U}_i^{(1)}),\\
(\sigma_2)_{,i} &= \rho_{02}\ddot{u}_i + \rho_{22}\ddot{U}_i^{(2)} - b_2(\dot{u}_i - \dot{U}_i^{(2)}), \qquad (4)
\end{aligned}
$$

where the comma preceding an index indicates spatial differentiation, $b_1 = \phi_1\phi_{10}\eta/\kappa_1$ and $b_2 = \phi_2\phi_{20}\eta/\kappa_2$ are the viscous couplings between the pore fluid and skeleton, and ρ_{ij} are five density parameters, given in Appendix A.

By substituting eq. (2) into (4), we obtain

$$
\begin{aligned}
&N\nabla^2\mathbf{u} + (A+N)\nabla\epsilon + Q_1\nabla(\eta^{(1)} + \phi_2\varsigma) + Q_2\nabla(\eta^{(2)} - \phi_1\varsigma)\\
&\quad = \rho_{00}\ddot{\mathbf{u}} + \rho_{01}\ddot{\mathbf{U}}^{(1)} + \rho_{02}\ddot{\mathbf{U}}^{(2)} + b_1(\dot{\mathbf{u}} - \dot{\mathbf{U}}^{(1)}) + b_2(\dot{\mathbf{u}} - \dot{\mathbf{U}}^{(2)}),\\
&Q_1\nabla\epsilon + R_1\nabla(\eta^{(1)} + \phi_2\varsigma) = \rho_{01}\ddot{\mathbf{u}} + \rho_{11}\ddot{\mathbf{U}}^{(1)} - b_1(\dot{\mathbf{u}} - \dot{\mathbf{U}}^{(1)}),\\
&Q_2\nabla\epsilon + R_2\nabla(\eta^{(2)} - \phi_1\varsigma) = \rho_{02}\ddot{\mathbf{u}} + \rho_{22}\ddot{\mathbf{U}}^{(2)} - b_2(\dot{\mathbf{u}} - \dot{\mathbf{U}}^{(2)}). \quad (5)
\end{aligned}
$$

Eqs (3) and (5) constitute the basic equations for wave propagation in cracked porous media. They hold for uniform porosity because the average displacements of the solid and fluid phases are used as Lagrangian coordinates and the respective stress components are used as generalized forces.

In the non-uniform case, the relative fluid displacement $\mathbf{w}^{(m)}$, the total stress τ_{ij} and pore-fluid pressure P_{fm} must be used and are expressed by

$$
\begin{aligned}
\mathbf{w}^{(m)} &= \phi_m(\mathbf{U}^{(m)} - \mathbf{u}),\\
\tau_{ij} &= \sigma_{ij} + (\sigma_1 + \sigma_2)\delta_{ij},\\
P_{fm} &= -\frac{1}{\phi_m}\sigma_m, \qquad (6)
\end{aligned}
$$

where $m = 1, 2$ refer to the host medium and inclusions, respectively.

Using eq. (2), we have

$$
\begin{aligned}
\tau_{ij} &= 2\mu_b\epsilon_{ij} + (\lambda_c\epsilon - \alpha_1 M_1(\xi^{(1)} - \phi_1\phi_2\varsigma)\\
&\quad - \alpha_2 M_2(\xi^{(2)} + \phi_1\phi_2\varsigma))\delta_{ij},\\
P_{f1} &= -\alpha_1 M_1\epsilon + M_1(\xi^{(1)} - \phi_1\phi_2\varsigma),\\
P_{f2} &= -\alpha_2 M_2\epsilon + M_2(\xi^{(2)} + \phi_1\phi_2\varsigma), \qquad (7)
\end{aligned}
$$

where $\xi^{(m)} = -\nabla\cdot\mathbf{w}^{(m)} = -\phi_m(\eta^{(m)} - \epsilon)$ are the two variations of fluid content relative to the solid, μ_b is the dry-rock shear modulus, and λ_c, α_1, α_2, M_1 and M_2 are stiffness coefficients given in Appendix A. Eq. (7) is the correct one for describing wave propagation in an inhomogeneous media because it is consistent with Darcy's law and the BCs at interfaces separating media with different properties.

3 PLANE-WAVE SOLUTION

Considering time harmonic oscillations with a Fourier convention $\exp[-\mathrm{i}\omega t]$ and solving eq. (3), we obtain

$$
\begin{aligned}
&\varsigma = d_1\epsilon + d_2\eta^{(1)} + d_3\eta^{(2)},\\
&d_1 = (\phi_1 Q_2 - \phi_2 Q_1)/L_d,\ d_2 = -\phi_2 R_1/L_d,\ d_3 = \phi_1 R_2/L_d, \qquad (8)
\end{aligned}
$$

with

$$
\begin{aligned}
L_1 &= \left(\frac{3}{8} + \frac{\phi_{20}}{2\phi_{10}}\ln\frac{L+R_0}{R_0}\right)\phi_1^2\phi_2\rho_f R_0^2,\\
L_2 &= \left(\frac{3\eta}{8\kappa_2} + \frac{\eta}{2\kappa_1}\ln\frac{L+R_0}{R_0}\right)\phi_{20}\phi_1^2\phi_2 R_0^2,\\
L_d &= L_1\omega^2 + L_2\mathrm{i}\omega + \phi_2^2 R_1 + \phi_1^2 R_2, \qquad (9)
\end{aligned}
$$

where ω is the angular frequency and i is the imaginary unit. When $R_0 = +\infty$, the coefficients d_i ($i = 1, 2, 3$) become zero, and hence the mesoscopic fluid-flow effect disappears.

Substituting eq. (8) into eq. (5) yields

$$
\begin{aligned}
&N\nabla^2\mathbf{u} + (A + N + Zd_1)\nabla\epsilon + (Q_1 + Zd_2)\nabla\eta^{(1)}\\
&\quad + (Q_2 + Zd_3)\nabla\eta^{(2)}\\
&\quad = \rho_{00}\ddot{\mathbf{u}} + \rho_{01}\ddot{\mathbf{U}}^{(1)} + \rho_{02}\ddot{\mathbf{U}}^{(2)} + b_1(\dot{\mathbf{u}} - \dot{\mathbf{U}}^{(1)}) + b_2(\dot{\mathbf{u}} - \dot{\mathbf{U}}^{(2)}),\\
&(Q_1 + R_1\phi_2 d_1)\nabla\epsilon + (R_1 + R_1\phi_2 d_2)\nabla\eta^{(1)} + R_1\phi_2 d_3\nabla\eta^{(2)}\\
&\quad = \rho_{01}\ddot{\mathbf{u}} + \rho_{11}\ddot{\mathbf{U}}^{(1)} - b_1(\dot{\mathbf{u}} - \dot{\mathbf{U}}^{(1)}),\\
&(Q_2 - R_2\phi_1 d_1)\nabla\epsilon - R_2\phi_1 d_2\nabla\eta^{(1)} + (R_2 - R_2\phi_1 d_3)\nabla\eta^{(2)}\\
&\quad = \rho_{02}\ddot{\mathbf{u}} + \rho_{22}\ddot{\mathbf{U}}^{(2)} - b_2(\dot{\mathbf{u}} - \dot{\mathbf{U}}^{(2)}), \qquad (10)
\end{aligned}
$$

where $Z = Q_1\phi_2 - Q_2\phi_1$.

Based on the Helmholtz decomposition, the displacement vectors $\mathbf{u}$, $\mathbf{U^{(1)}}$ and $\mathbf{U^{(2)}}$ can be expressed in terms of potential functions φ_i and $\Psi_\mathbf{i}$ ($i = 0, 1, 2$) as follows,

$$
\begin{aligned}
&\mathbf{u} = \nabla\varphi_0 + \nabla\times\Psi_\mathbf{0},\ \mathbf{U}^{(1)} = \nabla\varphi_1 + \nabla\times\Psi_\mathbf{1},\\
&\mathbf{U}^{(2)} = \nabla\varphi_2 + \nabla\times\Psi_\mathbf{2}, \qquad (11)
\end{aligned}
$$

with

$$\begin{cases} \varphi_0 = A_0 \exp\left[\mathrm{i}(\mathbf{k_p}\cdot\mathbf{r} - \omega t)\right] \\ \varphi_1 = A_1 \exp\left[\mathrm{i}(\mathbf{k_p}\cdot\mathbf{r} - \omega t)\right] \\ \varphi_2 = A_2 \exp\left[\mathrm{i}(\mathbf{k_p}\cdot\mathbf{r} - \omega t)\right] \end{cases}, \quad \begin{cases} \Psi_0 = B_0 \exp\left[\mathrm{i}(\mathbf{k_s}\cdot\mathbf{r} - \omega t)\right] \\ \Psi_1 = B_1 \exp\left[\mathrm{i}(\mathbf{k_s}\cdot\mathbf{r} - \omega t)\right] \\ \Psi_2 = B_2 \exp\left[\mathrm{i}(\mathbf{k_s}\cdot\mathbf{r} - \omega t)\right] \end{cases} \tag{12}$$

where $\mathbf{k_p}$ and $\mathbf{k_s}$ are the wavenumbers of the compressional and shear waves, $\mathbf{r}$ is the space vector, and A_i and B_i are amplitudes, with subscripts $i = 0, 1, 2$ corresponding to the solid, and fluid phase in the host medium and inclusions (cracks), respectively.

Applying the divergence operator to (10), we obtain

$$\mathbf{H}\cdot\mathbf{A} = \mathbf{0}, \tag{13}$$

where we have used eqs (11) and (12), $\mathbf{A} = [A_0, A_1, A_2]^{\mathrm{T}}$, and the components of $\mathbf{H}$ are

$$\begin{cases} H_{11} = (A + 2N + Zd_1)k_p^2 - \rho_{00}\omega^2 - \mathrm{i}\omega(b_1 + b_2), \\ H_{12} = H_{21} = (Q_1 + Zd_2)k_p^2 - \rho_{01}\omega^2 + \mathrm{i}\omega b_1, \\ H_{13} = H_{31} = (Q_2 + Zd_3)k_p^2 - \rho_{02}\omega^2 + \mathrm{i}\omega b_2, \\ H_{22} = (R_1 + R_1\phi_2 d_2)k_p^2 - \rho_{11}\omega^2 - \mathrm{i}\omega b_1, \\ H_{23} = H_{32} = R_1\phi_2 d_3 k_p^2, \\ H_{33} = (R_2 - R_2\phi_1 d_3)k_p^2 - \rho_{22}\omega^2 - \mathrm{i}\omega b_2. \end{cases} \tag{14}$$

The equation $\det(\mathbf{H}) = 0$ gives three complex roots (denoted as k_1, k_2 and k_3) for the unknown wavenumbers, corresponding to the fast P wave (P1) and two slow P waves (P2 and P3). The related velocities, being complex, describe the attenuation characteristics.

Solving eq. (13), we obtain the relative relations between the amplitudes of two fluid-phase potentials and that of the solid phase for the specific k_i as,

$$\begin{pmatrix} A_1/A_0 \\ A_2/A_0 \end{pmatrix}\Bigg|_{k=k_i} = \begin{pmatrix} (H_{13}H_{21} - H_{11}H_{23})/(H_{12}H_{23} - H_{13}H_{22}) \\ (H_{11}H_{22} - H_{21}H_{12})/(H_{12}H_{23} - H_{13}H_{22}) \end{pmatrix}\Bigg|_{k=k_i} = \begin{pmatrix} \nu_i \\ \delta_i \end{pmatrix}. \tag{15}$$

For the shear wave, and based on eqs (10)–(12), we similarly have

$$\mathbf{Q}\cdot\mathbf{B} = \mathbf{0}, \tag{16}$$

where, $\mathbf{B} = [B_0, B_1, B_2]^{\mathrm{T}}$, and the components of $\mathbf{Q}$ are

$$\begin{cases} Q_{11} = Nk_s^2 - \rho_{00}\omega^2 - \mathrm{i}\omega(b_1 + b_2), \\ Q_{12} = Q_{21} = -\rho_{01}\omega^2 + \mathrm{i}\omega b_1, \\ Q_{13} = Q_{31} = -\rho_{02}\omega^2 + \mathrm{i}\omega b_2, \\ Q_{22} = -\rho_{11}\omega^2 - \mathrm{i}\omega b_1, \\ Q_{23} = Q_{32} = 0, \\ Q_{33} = -\rho_{22}\omega^2 - \mathrm{i}\omega b_2. \end{cases} \tag{17}$$

The equation $\det(\mathbf{Q}) = 0$ gives one complex wavenumber (denoted as k_4), corresponding to the shear wave (SV), and the relative-amplitude ratio is solved as

$$\begin{pmatrix} B_1/B_0 \\ B_2/B_0 \end{pmatrix} = \begin{pmatrix} -Q_{21}/Q_{22} \\ (Q_{21}Q_{12} - Q_{11}Q_{22})/(Q_{13}Q_{22}) \end{pmatrix} = \begin{pmatrix} \nu_4 \\ \delta_4 \end{pmatrix}. \tag{18}$$

Once k_i is determined, the corresponding phase velocity and attenuation factor are computed as (Carcione 2022)

$$V_i = \left[\mathrm{Re}\left(\frac{k_i}{\omega}\right)\right]^{-1}, \quad Q_i = \frac{\mathrm{Re}(k_i)}{2\mathrm{Im}(k_i)}, \quad i = 1, 2, 3, 4, \tag{19}$$

where, "Re" and "Im" denote real and imaginary parts and indexes 1 to 4 correspond to the wave modes P1, P2, P3 and SV, respectively. The attenuation factor defined in this way is the ratio between the total energy (strain plus kinetic) and the dissipated energy. The definition of Q as twice the strain energy divided by the dissipated energy, $Q_i = \dfrac{\mathrm{Re}[(\omega/k_i)^2]}{\mathrm{Im}[(\omega/k_i)^2]}$, can also be used, but it may yield negative values for slow waves, since the LFF and Biot mechanisms are losses associated with the kinetic energy.

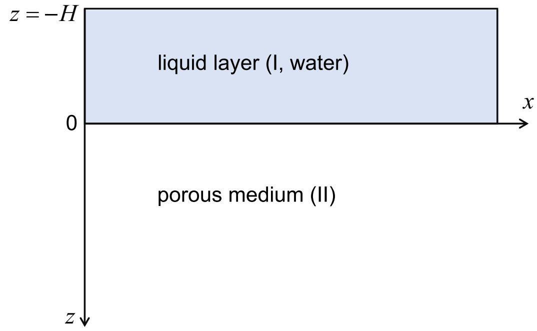

Figure 1. Geometry model of the problem.

4 SURFACE-WAVE PROPAGATION

We consider a liquid layer of thickness H (denoted as medium I) overlying a cracked double-porosity half-space (denoted as medium II), shown in Fig. 1, where the x-axis is along the interface and z-axis is in the direction of increasing depth into the porous medium. $z = 0$ is taken as the interface separating the liquid and the porous medium. Hence the region $-H < z < 0$ defines the liquid layer, whereas the cracked porous medium occupies the area $z > 0$. Because there is no shear wave in the liquid layer, Love waves do not propagate at the interface.

The equation of motion of the fluid in terms of potential Φ_0 is

$$\frac{\partial^2\Phi_0}{\partial x^2} + \frac{\partial^2\Phi_0}{\partial z^2} = \frac{1}{v_0^2}\frac{\partial^2\Phi_0}{\partial t^2}, \tag{20}$$

where $v_0 = (\lambda_0/\rho_0)^{1/2}$ is the velocity, with λ_0 and ρ_0 being the bulk modulus and density, respectively.

The solution of eq. (20) for surface-wave propagation is

$$\Phi_0 = [D_0\exp(kz\xi_0) + E_0\exp(-kz\xi_0)]\exp[\mathrm{i}(kx - \omega t)], \tag{21}$$

where D_0 and E_0 are the amplitudes, k is the horizontal wavenumber and $\xi_0 = (1 - c^2/v_0^2)^{1/2}$, with $c = \omega/k$ being the surface-wave velocity.

The displacement and stress are

$$\mathbf{u}_0 = (u_x, u_z)^{\mathrm{T}} = \nabla\Phi_0, \\ \tau_{xz} = 0, \qquad \tau_{zz} = -p_f = \lambda_0\left(\frac{\partial^2\Phi_0}{\partial x^2} + \frac{\partial^2\Phi_0}{\partial z^2}\right), \tag{22}$$

respectively.

On the other hand, the displacements of the solid and fluid in the porous medium are

$$u_x = \sum_{j=1}^{3}\frac{\partial\Phi_j}{\partial x} - \frac{\partial\Phi_4}{\partial z}, \qquad u_z = \sum_{j=1}^{3}\frac{\partial\Phi_j}{\partial z} + \frac{\partial\Phi_4}{\partial x},$$
$$U_x^{(1)} = \sum_{j=1}^{3}\nu_j\frac{\partial\Phi_j}{\partial x} - \nu_4\frac{\partial\Phi_4}{\partial z}, \quad U_z^{(1)} = \sum_{j=1}^{3}\nu_j\frac{\partial\Phi_j}{\partial z} + \nu_4\frac{\partial\Phi_4}{\partial x},$$
$$U_x^{(2)} = \sum_{j=1}^{3}\delta_j\frac{\partial\Phi_j}{\partial x} - \delta_4\frac{\partial\Phi_4}{\partial z}, \quad U_z^{(2)} = \sum_{j=1}^{3}\delta_j\frac{\partial\Phi_j}{\partial z} + \delta_4\frac{\partial\Phi_4}{\partial x}, \tag{23}$$

Table 1. Porous-medium properties.

	K_s (GPa)	μ_s (GPa)	ρ_s (kg/m^3)	ϕ_{10}	ϕ_{20}	c_1	κ_1 (darcy)	κ_2 (darcy)	R_0(m)
Rock	37.9	32.6	2650	0.25	0.32	11	0.1	100	0.03

Table 2. Fluid properties.

	K_f (GPa)	η_f (Pa·s)	ρ_f (kg/m^3)
Water	2.22	0.001	1000

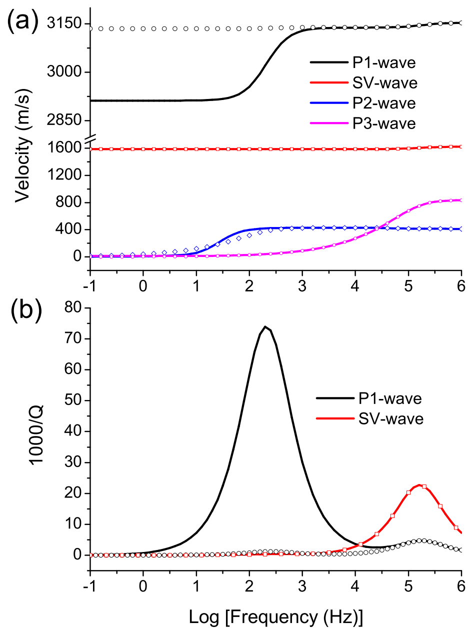

Figure 2. Phase velocities (a) and dissipation factors (b) of the body wave modes as a function of frequency ($\epsilon = 0.20$ and $\gamma = 0.002$). The solid lines represent the results in the presence of local fluid flow (LFF), whereas open symbols correspond to results without LFF.

where the potentials $\Phi_j (j = 1, \cdots, 4)$ represent the propagations of P1, P2, P3 and SV waves. For harmonic surface-wave propagation, they can be analytically expressed by

$$\Phi_j = D_j \exp[\mathrm{i}(kx - \omega t) - kz\xi_j],$$
$$\xi_j = \sqrt{1 - c^2/v_j^2},\ j = 1, 2, 3, 4 \tag{24}$$

where D_j are the amplitudes, $v_j = \omega/k_j$ are the complex velocities of the four body waves ($j = 1$, 2, 3 and 4 correspond to the P1, P2, P3, and SV waves). Using eqs (23) and (24), the total stress τ_{ij} and pore-fluid pressure P_{fm} can be obtained using eq. (7).

4.1 Boundary conditions

At the free surface of the liquid, defined by $z = -H$, we have

$$(\tau_{zz})_{\mathrm{I}} = 0. \tag{25}$$

Then, we obtain

$$E_0 = -D_0 \exp(-2kH\xi_0), \tag{26}$$

and hence eq. (21) is simplified as

$$\Phi_0 = D_0 \exp(-kH\xi_0)\Big\{\exp[k\xi_0(z + H)] - \exp[-k\xi_0(z + H)]\Big\} \times \exp[\mathrm{i}(kx - \omega t)]. \tag{27}$$

At the interface between the fluid layer and the porous medium, defined at $z = 0$, the BCs are given (Deresiewicz & Skalak 1963)

$$\begin{aligned} &(\tau_{xz})_{\mathrm{II}} = 0, \\ &(\tau_{zz})_{\mathrm{I}} = (\tau_{zz})_{\mathrm{II}}, \\ &(u_z)_{\mathrm{I}} = (u_z)_{\mathrm{II}} + (w_z^{(1)})_{\mathrm{II}} + (w_z^{(2)})_{\mathrm{II}}, \\ &(p_f)_{\mathrm{I}} - (P_{f1})_{\mathrm{II}} = Z_1(\dot{w}_z^{(1)})_{\mathrm{II}}, \\ &(p_f)_{\mathrm{I}} - (P_{f2})_{\mathrm{II}} = Z_2(\dot{w}_z^{(2)})_{\mathrm{II}}, \end{aligned} \tag{28}$$

where the first three equations represent the continuity of the normal and shear stresses and the conservation of mass, whereas the last two are conditions for the fluid pressure, where Z_1 and Z_2 are the so-called interface impedances. In particular, $Z_1 = Z_2 = 0$ and $Z_1 = Z_2 = \infty$ represent fully open and sealed BCs, respectively (Carcione *et al.* 2021). For intermediate values, they represent partially permeable boundaries (Nagy & Blaho 1994; Qi *et al.* 2021), which are not considered here.

The five BCs form a system of equations of order five on the unknown amplitudes $\mathbf{D} = [D_0, D_1, D_2, D_3, D_4]^T$ as follows,

$$\mathbf{MD} = \mathbf{0}, \tag{29}$$

where the elements of $\mathbf{M}$ are given in Appendix B.

4.2 Special cases

When $H = 0$, the BCs in eq. (28) become

$$\begin{aligned} &(\tau_{xz})_{\mathrm{II}} = 0, \\ &(\tau_{zz})_{\mathrm{II}} = 0, \\ &-(P_{f1})_{\mathrm{II}} = Z_1(\dot{w}_z^{(1)})_{\mathrm{II}}, \\ &-(P_{f2})_{\mathrm{II}} = Z_2(\dot{w}_z^{(2)})_{\mathrm{II}}, \end{aligned} \tag{30}$$

and the problem given in Fig. 1 reduces to the propagation of Rayleigh waves at the free surface of a cracked poroelastic half-space. The four BCs form a matrix equation of order four for the unknown amplitudes $\mathbf{D}^{(1)} = [D_1, D_2, D_3, D_4]^T$ as

$$\mathbf{M}^{(1)}\mathbf{D}^{(1)} = \mathbf{0}, \tag{31}$$

where the elements of $\mathbf{M}^{(1)}$ can be obtained by eliminating the first column and the third row of matrix $\mathbf{M}$ as,

$$\mathbf{M}^{(1)} = \begin{bmatrix} M_{01} & M_{02} & M_{03} & M_{04} \\ M_{11} & M_{12} & M_{13} & M_{14} \\ M_{31} & M_{32} & M_{33} & M_{34} \\ M_{41} & M_{42} & M_{43} & M_{44} \end{bmatrix}. \tag{32}$$

Alternatively, if $H = +\infty$, the problem corresponds to the propagation of pseudo-Stoneley (Scholte) wave at the interface between a liquid half-space and a cracked poroelastic half-space. In this case, $E_0 = 0$, and the potential Φ_0 is

$$\Phi_0 = D_0 \exp(kz\xi_0)\exp[\mathrm{i}(kx - \omega t)]. \tag{33}$$

At the interface, the BCs in eq. (28) remain the same, and the matrix equation becomes

$$\mathbf{M}^{(2)}\mathbf{D} = \mathbf{0}, \tag{34}$$

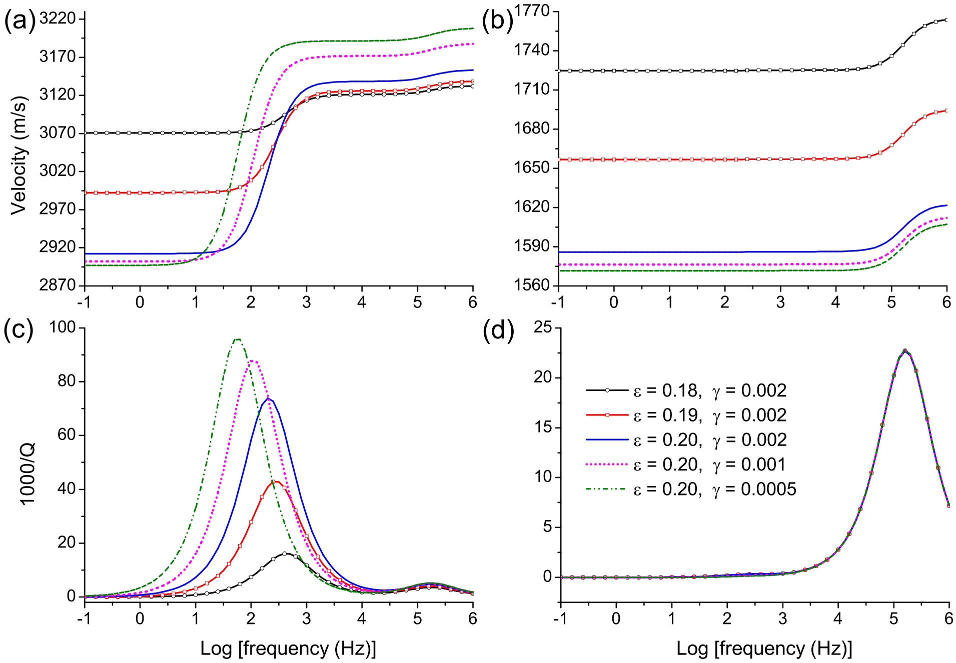

Figure 3. Phase velocities (a, b) and dissipation factors (c,d) of the P1 (a and c) and SV waves (b and d) as a function of frequency for different values of ϵ and γ. The LFF is present.

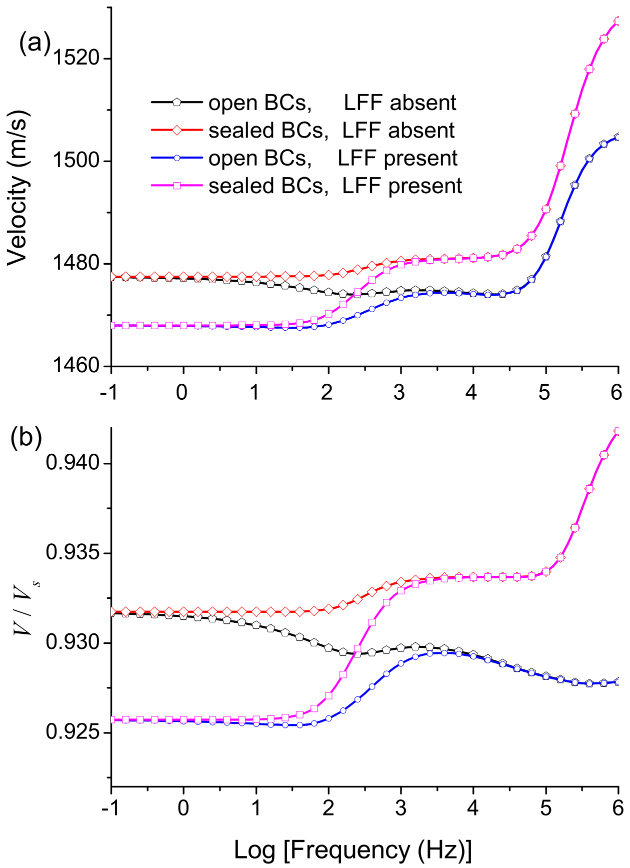

Figure 4. Phase velocity (a) and phase dimensionless velocity (b) of R1 wave, with respect to the shear wave velocity (V_S), as a function of frequency ($\epsilon = 0.20$ and $\gamma = 0.002$).

where the elements of $\mathbf{M}^{(2)}$ can be obtained from $\mathbf{M}$ by letting $H = +\infty$. Hence, the elements of the first column become

$$M_{00}^{(2)} = 0, \quad M_{10}^{(2)} = -\rho_0, \quad M_{20}^{(2)} = \xi_0,$$
$$M_{30}^{(2)} = M_{40}^{(2)} = -\rho_0, \tag{35}$$

whereas all the other elements of $\mathbf{M}^{(2)}$ remain the same as those of $\mathbf{M}$.

Note that the crack-double-porosity model reduces to the classic Biot theory when $f_2 = \phi_2 = 0$, in which case, the system of equation corresponding to (29) yields that derived by Feng & Johnson (1983), as shown in Appendix C.

4.3 Dispersion equation

A nontrivial solution of eq. (29) requires

$$\det(\mathbf{M}) = 0. \tag{36}$$

Eq. (36) involves transcendental functions and is nonlinear with respect to the unknown velocity c. We obtain a solution by using Muller's iteration method (Muller 1956). The existing complex solution indicates that propagation of the surface wave is inhomogeneous. The wave decays with depth in the porous half-space (increasing z for $z > 0$). Therefore, any solution of c requires a positive real part for $k\xi_j = \frac{\omega}{c}\xi_j$ given in eq. (24). The complex velocity c and wavenumber $k = \omega/c$ are then used to obtain the phase velocity and attenuation factor as (Carcione 2022),

$$V = \left[\mathrm{Re}\left(\frac{1}{c}\right)\right]^{-1} \quad \text{and} \quad Q = \frac{\mathrm{Re}(k)}{2\mathrm{Im}(k)}, \tag{37}$$

respectively.

Similarly, the dispersion equations for $H = 0$ and $H = +\infty$ are

$$\det(\mathbf{M}^{(1)}) = 0 \quad \text{and} \quad \det(\mathbf{M}^{(2)}) = 0, \tag{38}$$

respectively.

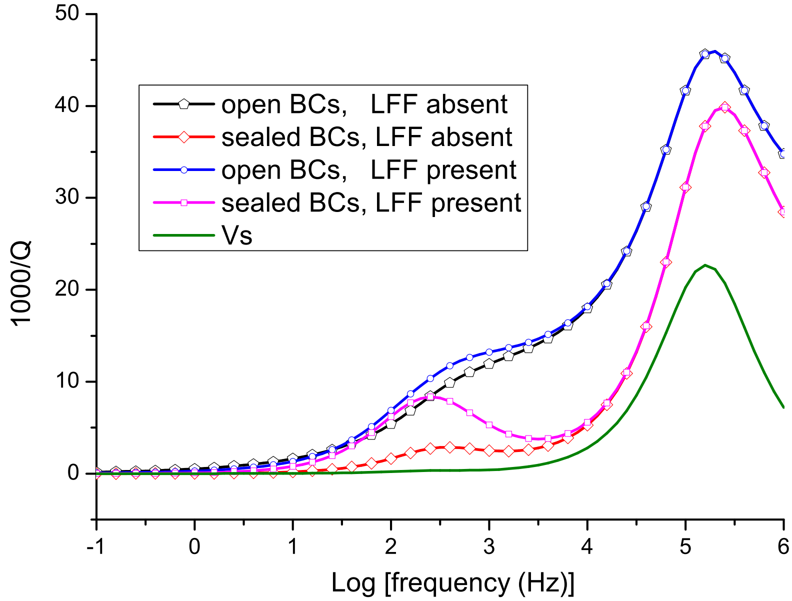

Figure 5. Dissipation factor of the R1 wave as a function of frequency.

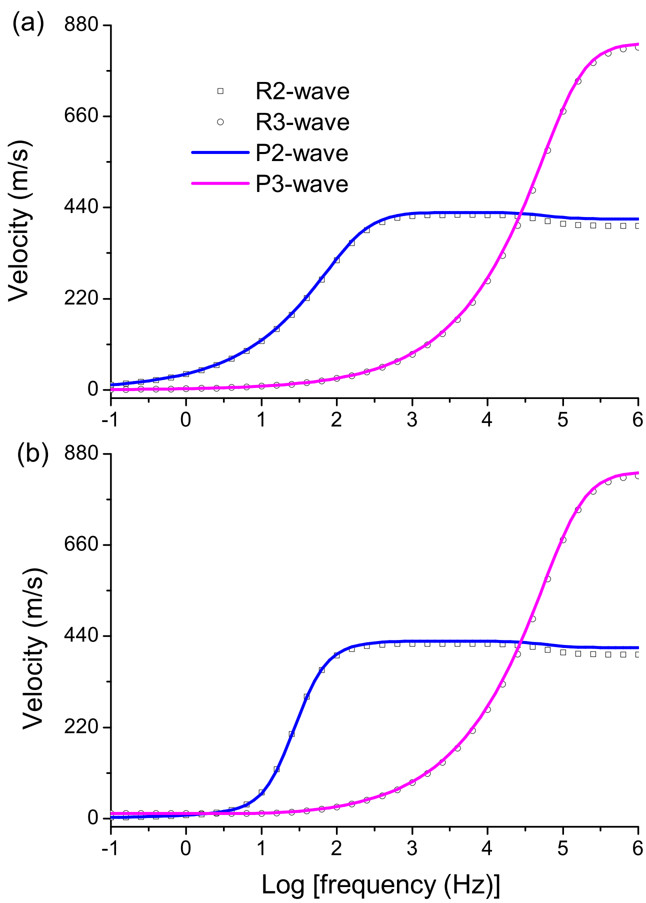

Figure 6. Phase velocities of the R2 and R3 waves as a function of frequency for sealed BCs, corresponding to the cases without LFF (a) and with LFF (b), respectively. For open BCs, these two waves don't exist.

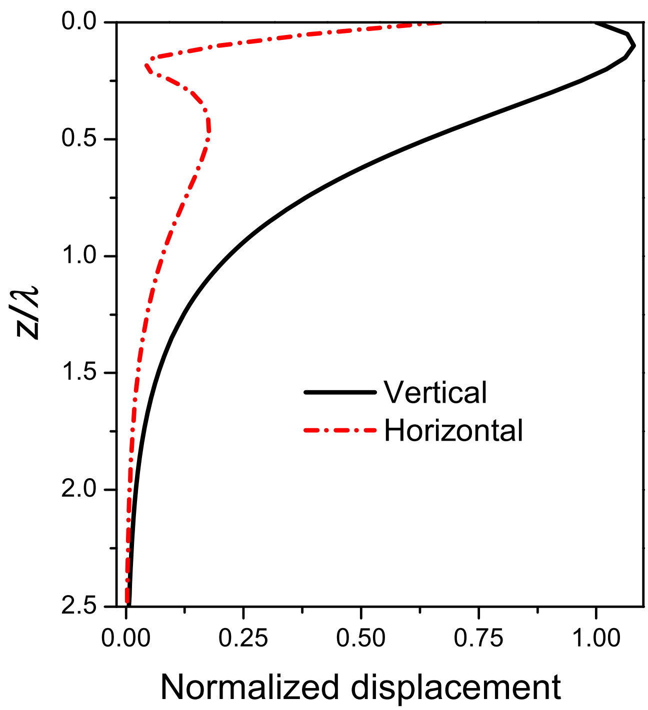

Figure 7. Absolute values of displacements of the R1 wave as a function of depth at 300 Hz. The displacements are normalized by the absolute vertical u_z at the surface ($z = 0$), and the depth is normalized by the R1 wavelength λ. The open-pore BCs are used and the LFF is present.

There can be more than one surface wave for the problem studied (Feng & Johnson 1983; Gubaidullin *et al.* 2004; Zhang *et al.* 2011; Sharma 2014). Feng & Johnson (1983) studied the surface-wave propagation at the interface between a fluid and a porous half-space

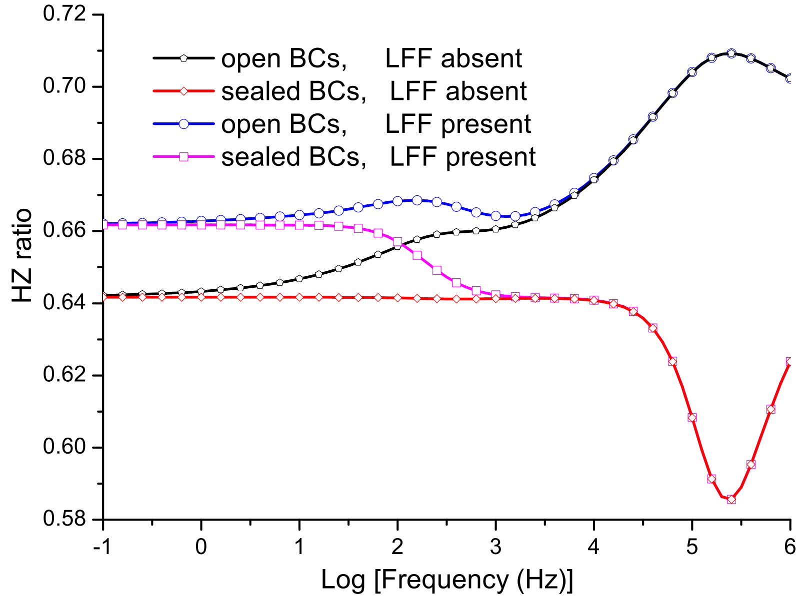

Figure 8. Ellipticity (HZ ratio) of the R1 wave as a function of frequency for the porous medium at the surface $z = 0$.

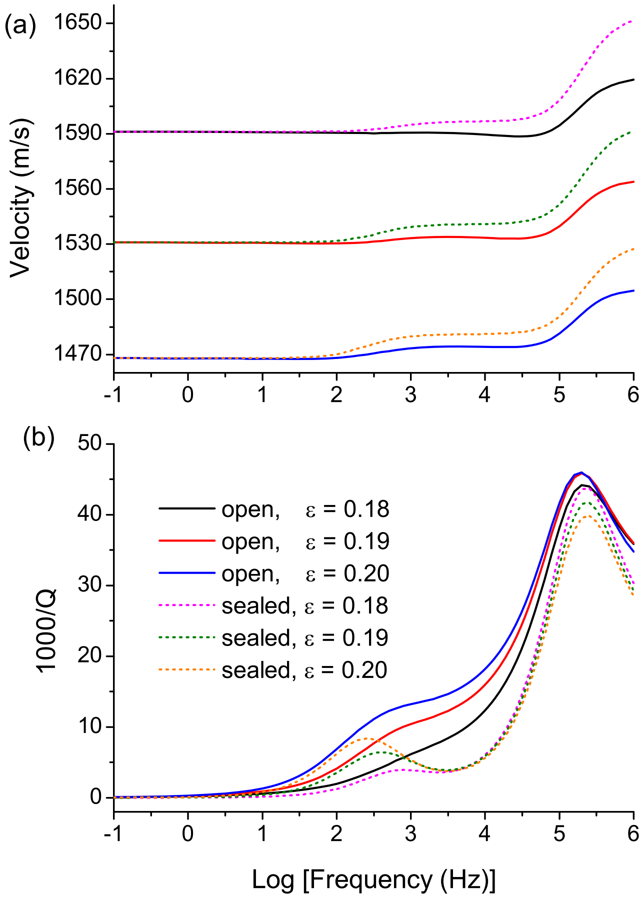

Figure 9. Effect of crack density ϵ on (a) velocity dispersion and (b) dissipation factor of the R1 wave. A constant $\gamma = 0.002$ is used. The LFF is present.

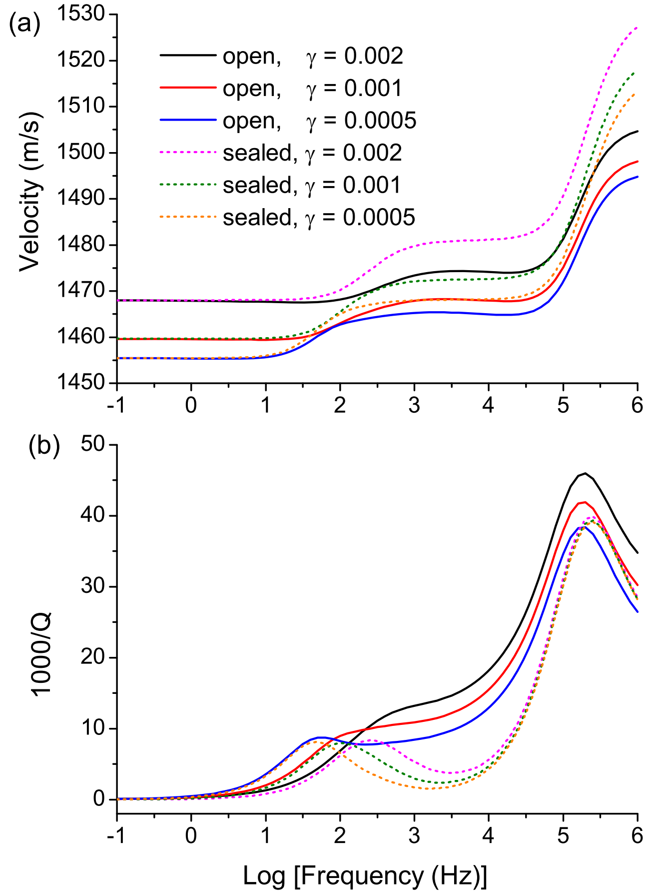

Figure 10. Effect of crack aspect ratio γ on (a) velocity dispersion and (b) dissipation factor of the R1 wave. A constant $\epsilon = 0.20$ is used. The LFF is present.

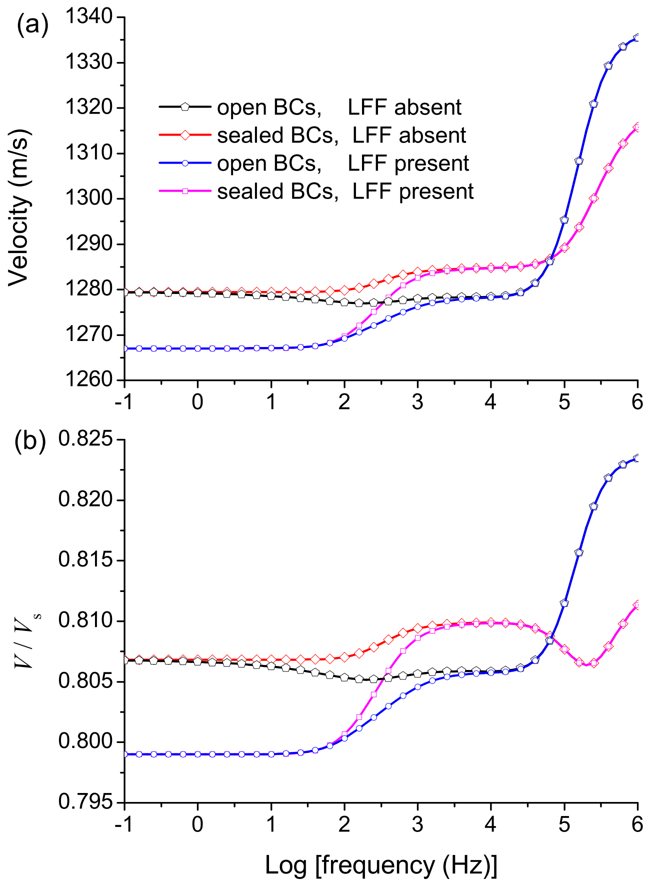

Figure 11. Phase velocity (a) and phase dimensionless velocity (b) of T1 wave, with respect to the shear wave velocity (V_S), as a function of frequency ($\epsilon = 0.20$ and $\gamma = 0.002$).

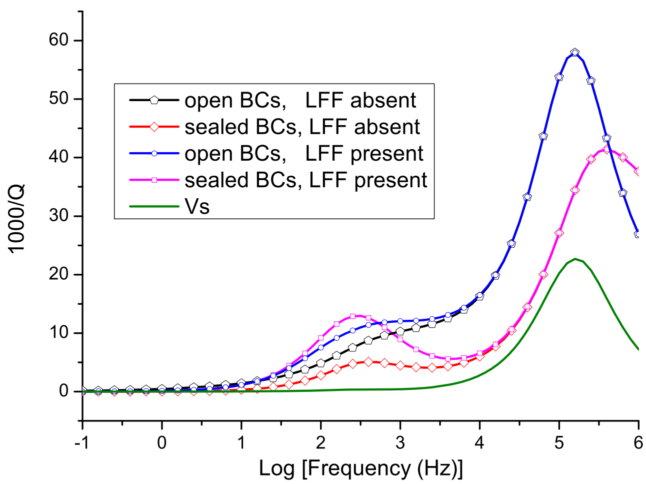

Figure 12. Dissipation factors of the T1 and shear waves as a function of frequency.

using Biot's theory, and confirmed the existence of a "true" surface wave and pseudo surface waves at the high frequency range, including the pseudo-Rayleigh and pseudo-Stoneley modes, depending on the BCs and medium parameters. The double-porosity model predicts two slow wave modes, and their interference with the fast P1 and SV waves makes the surface-wave propagation more complex.

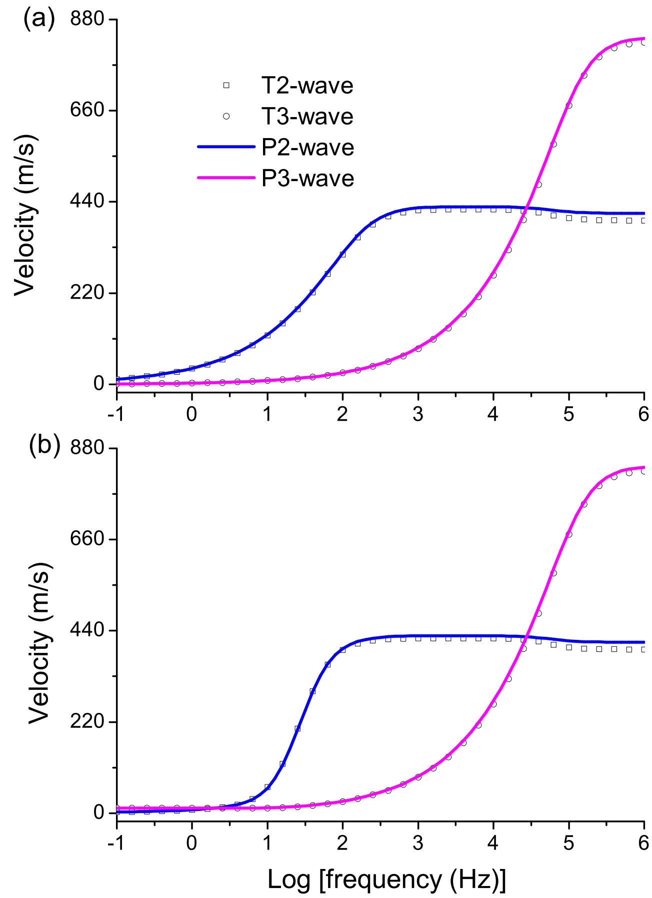

Figure 13. Phase velocities of the T2 and T3 waves as a function of frequency for sealed BCs, corresponding to the cases without LFF (a) and with LFF (b), respectively. For open BCs, these two waves don't exist.

4.4 Displacement motions

We obtain the displacements in the water layer I ($-H \le z < 0$) from eqs (22) and (27) as,

$$
\begin{aligned}
(u_x)^{\mathrm{I}} &= D_4 S_0 \mathrm{i} k \exp(-kH\xi_0) \\
&\quad \times \{\exp[k\xi_0(z+H)] - \exp[-k\xi_0(z+H)]\}\exp[\mathrm{i}(kx-\omega t)], \\
(u_z)^{\mathrm{I}} &= D_4 S_0 k \xi_0 \exp(-kH\xi_0) \\
&\quad \times \{\exp[k\xi_0(z+H)] + \exp[-k\xi_0(z+H)]\}\exp[\mathrm{i}(kx-\omega t)],
\end{aligned}
\tag{39}
$$

where $S_0 = D_0/D_4$ is the amplitude ratio.

Similarly, in the double-porosity medium II, defined by $z \ge 0$, the corresponding displacement components are

$$
\begin{aligned}
(u_x)^{\mathrm{II}} &= (u_x + w_x^{(1)} + w_x^{(2)})_{\mathrm{II}} = \sum_{j=1}^{3} \frac{\partial \Phi_j}{\partial x} t_j - \frac{\partial \Phi_4}{\partial z} t_4, \\
(u_z)^{\mathrm{II}} &= (u_z + w_z^{(1)} + w_z^{(2)})_{\mathrm{II}} = \sum_{j=1}^{3} \frac{\partial \Phi_j}{\partial z} t_j + \frac{\partial \Phi_4}{\partial x} t_4,
\end{aligned}
\tag{40}
$$

where $t_j = 1 - \phi_1 - \phi_2 + \phi_1 \nu_j + \phi_2 \delta_j, j = 1, 2, 3, 4$. Substituting eq. (24) into eq. (40), we have

$$
\begin{aligned}
(u_x)^{\mathrm{II}} &= \mathrm{i}|\beta_x|\exp[\mathrm{i}\arg(\beta_x)]\exp[\mathrm{i}(kx-\omega t)], \\
(u_z)^{\mathrm{II}} &= -|\beta_z|\exp[\mathrm{i}\arg(\beta_z)]\exp[\mathrm{i}(kx-\omega t)],
\end{aligned}
\tag{41}
$$

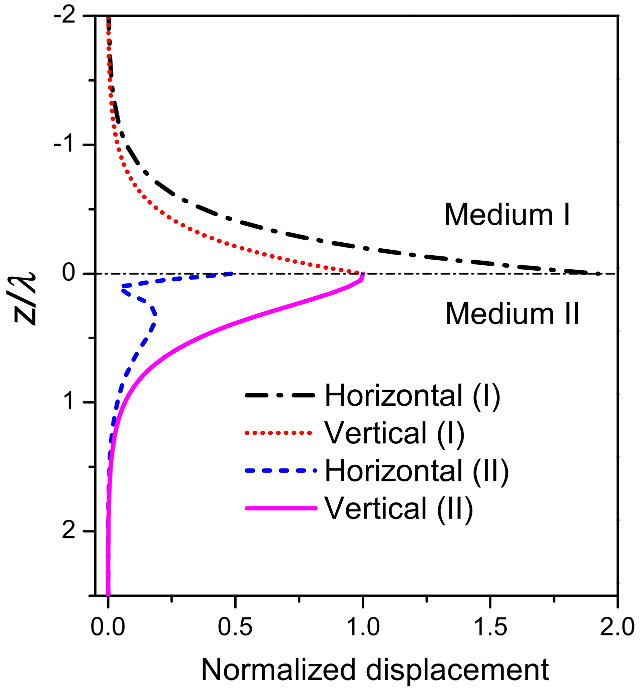

Figure 14. Absolute values of displacements of the T1 wave as a function of depth at 300 Hz. The displacements are normalized by the absolute vertical u_z at the surface ($z = 0$) in the double-porosity medium, and the depth is normalized by the pseudo-Stoneley wavelength λ. The open-pore BCs are used and the LFF is present.

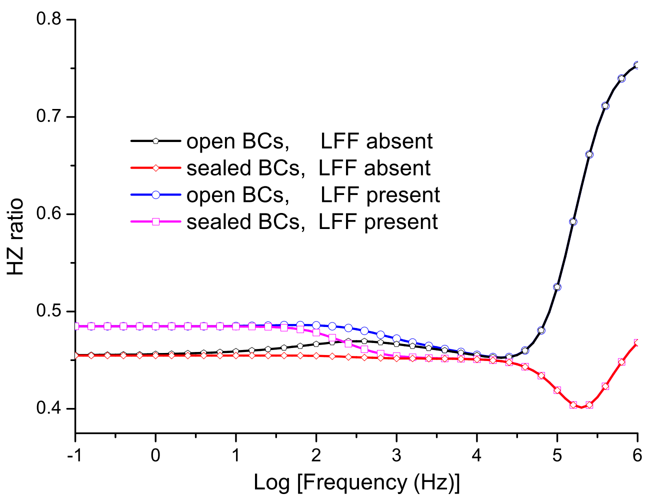

Figure 15. Ellipticity (HZ ratio) of the T1 wave as a function of frequency for the porous medium at the interface $z = 0$.

where

$$\beta_x = kD_4 \left(\sum_{j=1}^{3} t_j S_j \exp(-kz\xi_j) - \mathrm{i}t_4\xi_4 \exp(-kz\xi_4) \right),$$

$$\beta_z = kD_4 \left(\sum_{j=1}^{3} t_j S_j \xi_j \exp(-kz\xi_j) - \mathrm{i}t_4 \exp(-kz\xi_4) \right), \tag{42}$$

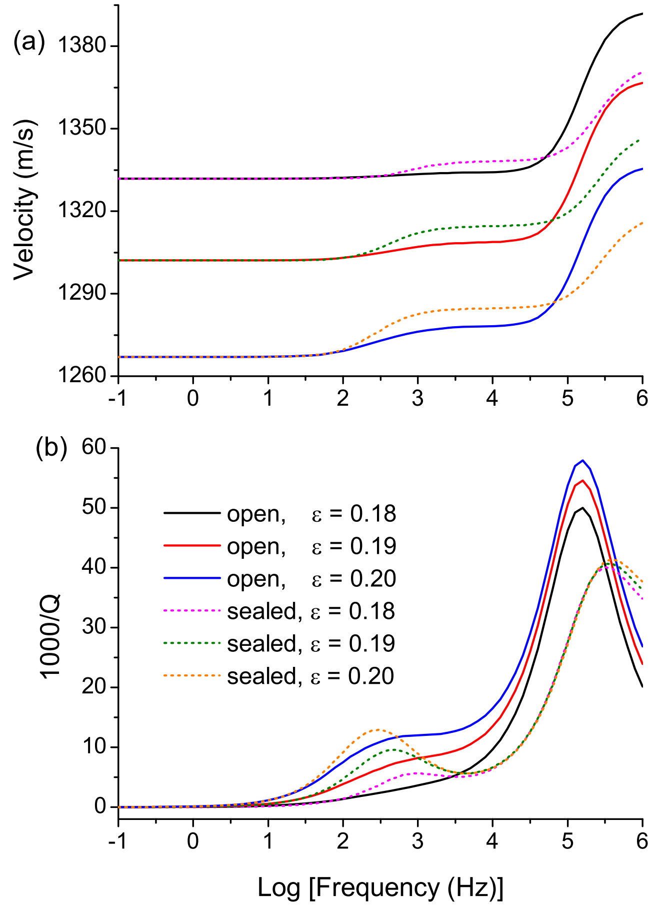

Figure 16. Effect of crack density ϵ on (a) velocity dispersion and (b) dissipation factor of the T1 wave. A constant $\gamma = 0.002$ is used. The LFF is present.

and $S_j = D_j/D_4$, which can be obtained from the singular system of BCs (29) as

$$\begin{bmatrix} M_{00} & M_{01} & M_{02} & M_{03} \\ M_{10} & M_{11} & M_{12} & M_{13} \\ M_{20} & M_{21} & M_{22} & M_{23} \\ M_{30} & M_{31} & M_{32} & M_{33} \end{bmatrix} \begin{bmatrix} S_0 \\ S_1 \\ S_2 \\ S_3 \end{bmatrix} = - \begin{bmatrix} M_{04} \\ M_{14} \\ M_{24} \\ M_{34} \end{bmatrix}, \tag{43}$$

for $H \neq 0$ including the special case of $H = +\infty$. For $H = 0$, we have

$$\begin{bmatrix} M_{01} & M_{02} & M_{03} \\ M_{11} & M_{12} & M_{13} \\ M_{31} & M_{32} & M_{33} \end{bmatrix} \begin{bmatrix} S_1 \\ S_2 \\ S_3 \end{bmatrix} = - \begin{bmatrix} M_{04} \\ M_{14} \\ M_{34} \end{bmatrix}. \tag{44}$$

The oscillating particles described by eq. (41) are along an elliptical path, and the corresponding ellipticity (the absolute ratio between the horizontal and vertical displacements) is defined as

$$HZ = \frac{|\beta_x|}{|\beta_z|}, \tag{45}$$

which gives the aspect ratio of the particle-motion ellipse.

5 EXAMPLES

We consider the properties given in Table 1, taken from Tang *et al.* (2012) and Zhang *et al.* (2019). The fluid is water and its properties are given in Table 2 (Gurevich *et al.* 2004). The volume fraction $f_2 = \phi_2/\phi_{20}$, where $\phi_2 = \phi_c = 2\pi\varepsilon\gamma$ is the crack porosity, with ε

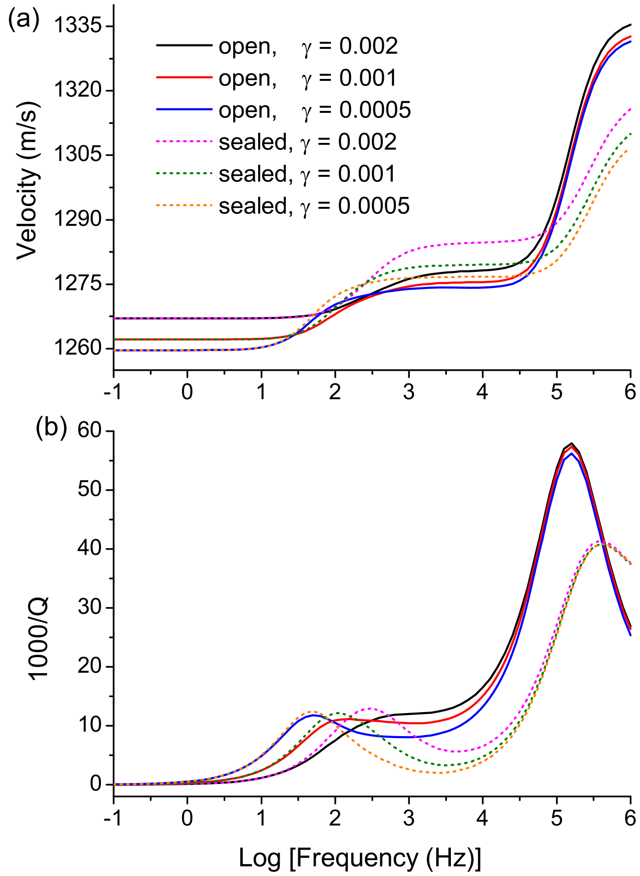

Figure 17. Effect of crack aspect ratio γ on (a) velocity dispersion and (b) dissipation factor of the T1 wave. A constant $\epsilon = 0.20$ is used. The LFF is present.

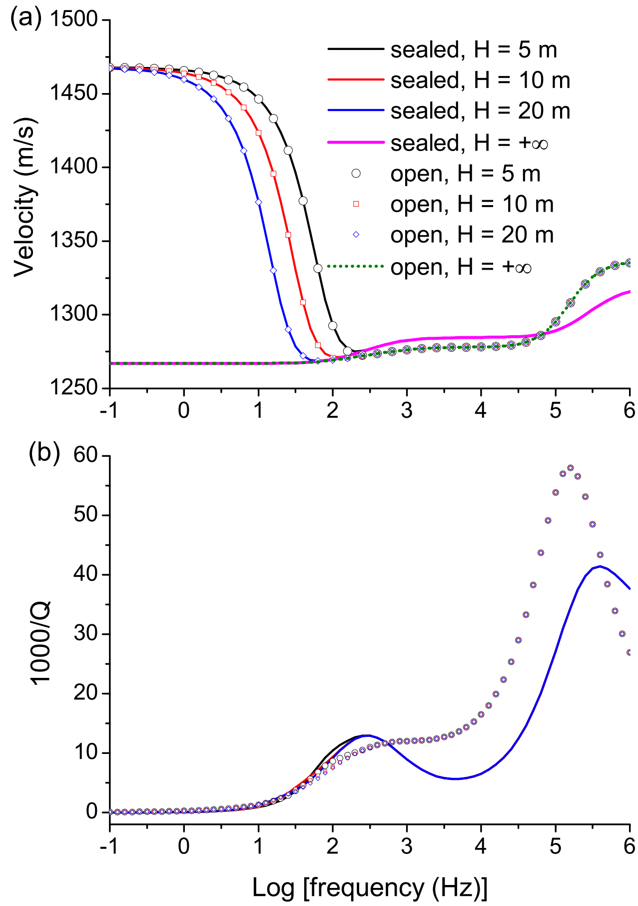

Figure 18. Phase velocity (a) and dissipation factor (b) of the fundamental mode with frequency at three different values of H ($\epsilon = 0.20$, $\gamma = 0.002$). The results of $H = +\infty$ correspond to those given in Figs 11 and 12. The LFF is present.

and γ being the crack density and aspect ratio, respectively (Zhang *et al.* 2019). In the following, we consider $\varepsilon = 0.2$ and $\gamma = 0.002$ (Tang *et al.* 2012).

Fig. 2 shows the phase velocities and dissipation factors of the body waves as a function of frequency. We observe that the LFF affects the P1-wave propagation significantly, inducing a significant attenuation peak between 10 Hz and 10 kHz, and consequently a velocity dispersion. Hence, at low frequencies, the P1-wave velocity becomes smaller than that when LFF is absent. At high frequencies, the effect of LFF disappears and the Biot global flow plays an important role, causing an attenuation peak. As a contrast, the LFF hardly affects the propagation of the P3 and SV modes. Considering that the surface waves result from the interference among the body waves, their propagation will definitely be influenced by the LFF mechanism.

The effects of crack density ε and aspect ratio γ on the propagation of P1 and SV waves are displayed in Fig. 3. For the P1 wave, the crack density mainly affects the amount of attenuation and velocity dispersion at low frequencies, whereas the aspect ratio is the main factor affecting the location of the relaxation peak. A higher crack density implies stronger attenuation, and a smaller aspect ratio moves the peak to low frequencies. For the SV wave, an increasing crack density implies a lower velocity, whereas the influence of the aspect ratio is opposite but not significant.

5.1 Waves at the surface of a double-porosity medium

First, we consider $H = 0$ to study the Rayleigh-type waves at the free surface of the double-porosity medium. The theory predicts three modes, denoted as R1, R2 and R3, respectively. The R1 wave propagates slower than the shear wave, but faster than the two slow P2 and P3 waves, which leaks its energy during the propagation and corresponds to the pseudo-Rayleigh wave. The R2 and R3 modes resemble the P2 and P3 waves and do not exist if the BCs are open. The results are consistent with those of Zhang *et al.* (2011), where they similarly found another slow surface mode for sealed and partially sealed BCs using the classical Biot equations. This mode is a true Stoneley wave because it has the smallest velocity and is not leaky.

Fig. 4 shows the phase velocity of the R1 wave as a function of frequency, and the corresponding dissipation factor is displayed in Fig. 5. It is evident that this wave propagates slower and is more attenuated than the SV wave (see Figs 4b and 5). The LFF mainly affects its propagation at frequencies less than 10 kHz, inducing a higher attenuation, particularly over the frequency band between 10 Hz and 1 kHz, and consequently giving a smaller phase velocity. The phenomenon is similar to the propagation of body waves in Fig. 2, because the LFF mechanism mainly occurs at the mesoscopic scale. At high frequencies, the phase velocity with sealed-pore BCs is higher than that with open-pores. But at the very low frequencies, they are identical, since in this case, the two slow waves do not

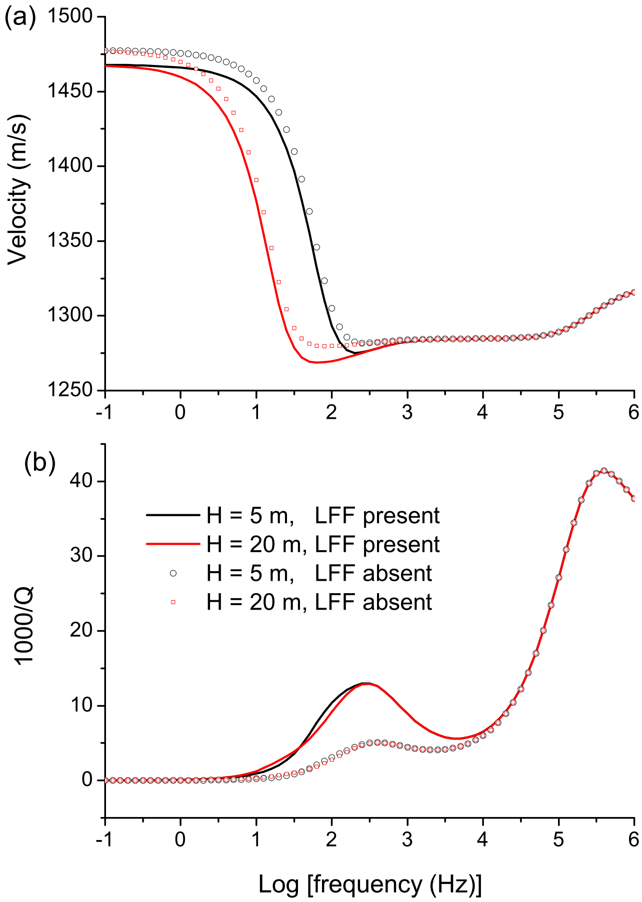

Figure 19. Phase velocity (a) and dissipation factor (b) of the fundamental mode with frequency at two values of H for sealed BCs ($\epsilon = 0.20$, $\gamma = 0.002$). The open symbols represent the results without LFF, whereas the solid lines are the results in the presence of LFF.

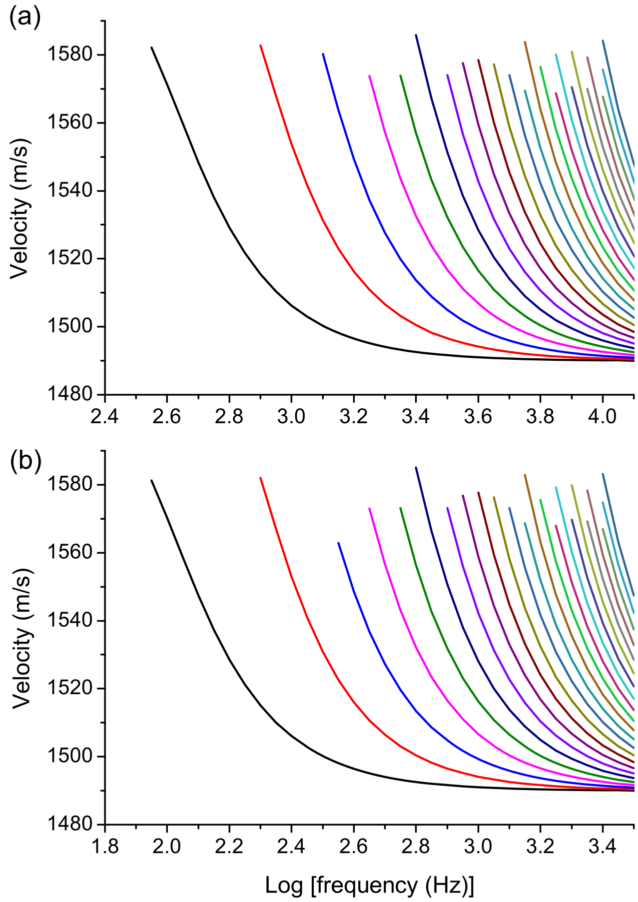

Figure 20. Phase velocities of the higher-order surface modes for $H = 5$ m (a) and $H = 20$ m (b), respectively. The sealed BCs are used and the LFF is present ($\epsilon = 0.20$, $\gamma = 0.002$).

propagate and the free surface becomes equivalent to the elastic one. Moreover, the open-pore BCs imply a higher attenuation of the pseudo-Rayleigh wave than that of the sealed-pore BCs, possibly due to the energy transfer between the fast and slow wave modes. Fig. 6 shows the phase velocities of the R2 and R3 modes as a function of frequency for sealed BCs. Irrespective of whether the LFF is present or absent, these two modes resemble the slow P2 and P3 waves, respectively, which are dispersive at low frequencies and become wavelike at high frequencies. For open BCs, we find no such waves. A similar true surface mode was confirmed in Zhang *et al.* (2011) by using the classical Biot theory.

Fig. 7 shows the displacements of R1 wave as a function of a dimensionless depth at a frequency of 300 Hz. The displacements decrease with increasing depth, due to the energy decay, and critical depth is approximately 2.0 times of the pseudo-Rayleigh wavelength. The vertical displacement predominates in the propagation, and exhibits a maximum at a depth of approximately one fifth the R1 wavelength λ, around which the horizontal displacement approaches zero, indicating that, the vertical and horizontal displacements are out of phase by approximately 90°. The results are quite similar as those of Qiu *et al.* (2019), and imply a retrograde elliptical motion of the particles near the surface. When the depth is larger than 0.2λ, the trajectory becomes clockwise (prograde). Fig. 8 further shows the variation of the ellipticity (HZ ratio) with frequency at the surface. The effects of the LFF and BCs are observed at low and high frequencies, respectively. At low frequencies, the presence of the LFF increases the ellipticity, whereas at high frequencies, the sealed BCs yield a smaller ellipticity. The HZ ratio increases with increasing frequency for open BCs, unlike the sealed case. The averaged HZ ratio is approximately 0.65.

Figs 9 and 10 show the effects of the crack density ϵ and aspect ratio γ on velocity dispersion and dissipation of the R1 wave. For both sealed and open BCs, the higher the ϵ is the lower the phase velocity of the R1 wave is and the higher the mesoscopic attenuation between 10 Hz and 10 kHz. Increasing ϵ significantly decreases the shear wave velocity, as shown in Fig. 3b, and the superposition with the other body waves implies a low pseudo-Rayleigh velocity. Increasing ϵ also enhances the P1-wave attenuation at low frequencies (see Fig. 3c), and consequently the attenuation of the R1 wave. On the other hand, increasing the aspect ratio γ, the velocity of the R1 wave increases, but the variations are not significant as those in Fig. 9. The relaxation frequency of the mesoscopic-scale attenuation also increases, but the amount of attenuation is not evidently affected. The reason is due to the fact that increasing γ implies a higher shear-wave velocity and moves the relaxation peak to higher frequencies. The variations in attenuation and velocity of the body waves are smaller than those for ϵ between 0.18 to 0.2, and hence the corresponding variations of the R1 wave are relatively small. We then conclude that the crack density mainly affects the amount of attenuation, whereas the crack aspect ratio is the main factor

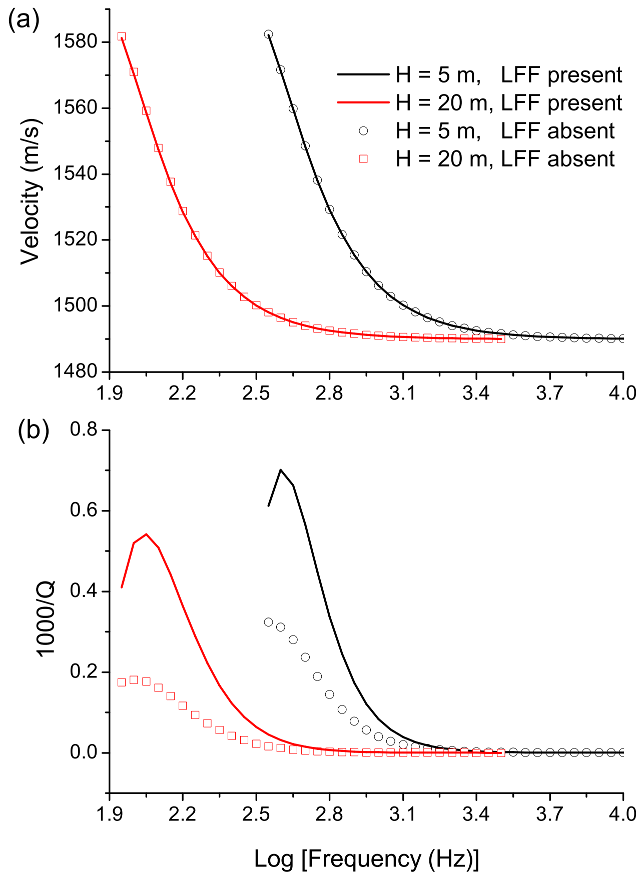

Figure 21. Phase velocity (a) and dissipation factor (b) of the first-order mode with frequency at two values of H for sealed BCs (ϵ = 0.20, γ = 0.002). The open symbols represent the results without LFF, whereas the solid lines are the results in the presence of LFF.

affecting the location of the relaxation peak, in agreement with effects on the body waves (Zhang *et al.* 2019).

5.2 Waves at the liquid/double-porosity medium interface

Next, we consider $H = +\infty$, corresponding to the propagation of Stoneley-type waves at the interface between water and poroelastic half-spaces. The theory confirms the existence of three modes, denoted as T1, T2 and T3, respectively. The T1 wave propagates slower than the fluid velocity, but faster than the two slow modes, which is a pseudo-Stoneley wave, since it is leaky. The two T2 and T3 waves are quite similar to the R2 and R3 modes and resemble the P2 and P3 waves, respectively. They exist only for sealed BCs.

Figs 11 and 12 show the phase velocity and dissipation factor of T1 wave as a function of frequency. Both the LFF and BCs affect the propagation of this wave significantly, in a similar manner as those on R1 wave, i.e., the BCs affect the propagation at high frequencies, whereas the effect of LFF is mainly observed at frequencies lower than 10 kHz. The LFF induces more attenuation on the frequency band between 10 Hz and 10 kHz, and consequently the velocity dispersion. At high frequencies, the sealed BCs yield a smaller velocity than the open-pore ones, unlike the results for the R1 wave. Moreover, the pseudo-Stoneley wave has a smaller velocity but stronger attenuation peaks than those of the pseudo-Rayleigh wave. It should propagate slower than the acoustic wave in water ($v_0 = \sqrt{\lambda_0/\rho_0}$ = 1490 m/s). Fig. 13 shows the phase velocities of the two slow T2 and T3 modes. Irrespective of whether the LFF is present or absent, these two waves resemble the P2 and P3 waves and exist only for sealed BCs. Using the classical high-frequency Biot theory, Feng & Johnson (1983) predicted a similar slow surface mode. It propagates slower than the Biot slow wave and is not leaky, i.e., it is a true Stoneley wave. As stated in Feng & Johnson (1983), this Stoneley mode is asymptotically the bulk slow wave. Due to the existence of two slow waves in the double-porosity theory, the surface-wave dispersion equation gives two slow Stoneley modes.

Fig. 14 shows the displacements of T1 wave as a function of depth when the frequency is 300 Hz. The vertical displacements in both the water and porous half-spaces are continuous at the interface, consistent with the BCs, whereas the horizontal displacements are not. The horizontal displacement in water is much larger. The critical depth is approximately 1.5 times the pseudo-Stoneley wavelength in both half-spaces, indicating that the wave decays faster in water. Similar as Fig. 7, a sharp variation of the horizontal displacement in the porous half-space can also be observed, suggesting the change in trajectories of the particle motions, whereas it is not evident in water. Fig. 15 shows the variations of the ellipticity (HZ ratio) with frequency at $z = 0$. The T1 wave has a relatively smaller ellipticity than the R1 wave given in Fig. 8, which are similarly affected by the LFF and BCs. At high frequencies, the ellipticity with open BCs increases significantly, possibly due to conversion between fast and slow modes through the open pores.

The crack density and aspect ratio affect the propagation of pseudo-Stoneley wave in a similar manner as that of the R1 wave, as shown in Figs 16 and 17. For both BCs, the phase velocity decreases with increasing ϵ, whereas it increases as γ increases. ϵ mainly affects the amount of attenuation, whereas γ is the main factor determining the relaxation frequency of the mesoscopic attenuation. Unlike the propagation of the R1 wave, the sealed BCs can give a smaller pseudo-Stoneley velocity at high frequencies, and a stronger mesoscopic attenuation, when compared with the open BCs.

5.3 Waves at the interface between a liquid layer and a double-porosity half-space

Finally, we consider the general case of a finite thickness H of the water layer. Similar to the results of the interface between a water layer and an elastic solid, the theory predicts high-order surface modes. In addition, for sealed-pore BCs, the theory predicts two slow modes that are quite similar to the T2 and T3 waves given in Fig. 13. Those two modes resemble the bulk P2 and P3 waves, and are hardly affected by the water thickness H (and therefore not displayed).

Fig. 18 shows the phase velocity and dissipation factor of the fundamental mode with frequency for three values of H, when LFF is present. At the low-frequency limit, the phase velocity is much higher than that of $H = +\infty$ and tends towards an asymptotic value of 1467 m/s = 0.9257 V_S, which is the velocity of the pseudo-Rayleigh wave (R1) traveling along the free surface of a porous half-space, as given in Fig. 4. At high frequencies, the result overlaps that of $H = +\infty$, corresponding to the propagation of a pseudo-Stoneley wave, as in Fig. 11, which is dependent on the BCs. Consequently, a significant velocity-dispersion decrease is observed over intermediate frequencies, in particular between 0.1 and 300 Hz, unlike the case $H = +\infty$, even though the attenuation is less than the Biot peak at high frequencies. The dispersion location moves to low frequencies when H increases. The effect of the BCs

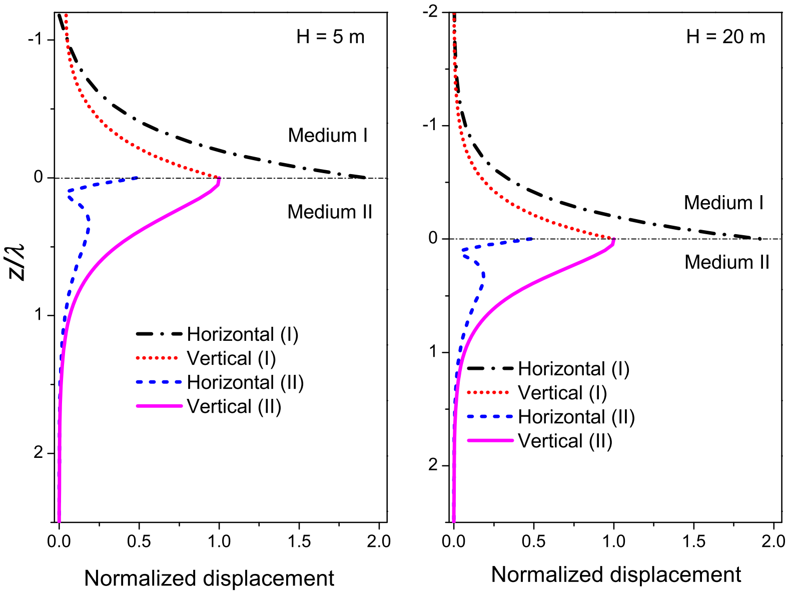

Figure 22. Absolute values of displacements of the fundamental mode (the pseudo-Stoneley) as a function of depth at 300 Hz for $H = 5$ m (left) and $H = 20$ m (right). The displacements are normalized by the absolute vertical u_z at the surface ($z = 0$) in the double-porosity medium, and the depth is normalized by the fundamental-mode wavelength λ. The open-pore BCs are used and the LFF is present.

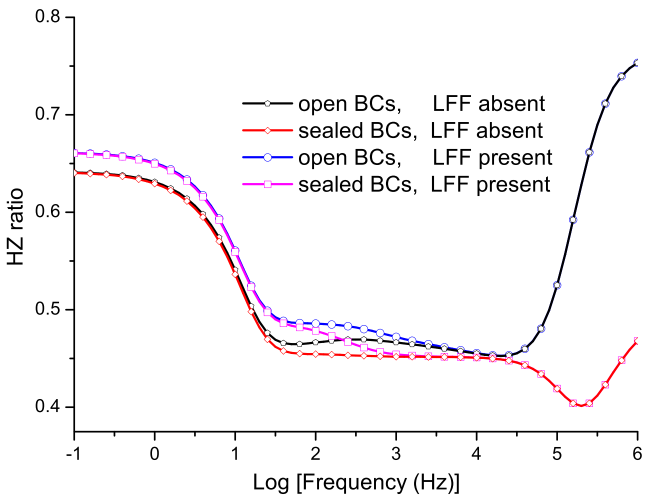

Figure 23. Ellipticity (HZ ratio) of the fundamental mode as a function of frequency for the porous medium at the interface $z = 0$ ($H = 20$ m).

is only significant at high frequencies, because at low frequencies, the slow wave modes don't propagate and the interface becomes equivalent to the water/elastic-medium one. The velocity is smaller than the fluid velocity $v_0 = 1490$ m/s, and hence the fundamental mode is a pseudo-Stoneley wave. Further comparisons, when the LFF is absent, are given in Fig. 19. We observe a significant dispersion at low frequencies. The presence of the LFF enhances the attenuation at frequencies between 10 Hz and 10 kHz. At the low-frequency limit, the velocity in the absence of LFF is larger, because the velocity of the pseudo-Rayleigh wave is higher, as displayed in Fig. 4.

Fig. 20 shows the velocity dispersion of the higher-order modes for $H = 5$ m and 20 m. The cut-off frequency regards the higher-order mode, and it increases as the order increases. The velocity of each mode is approximately equal to the shear-wave velocity

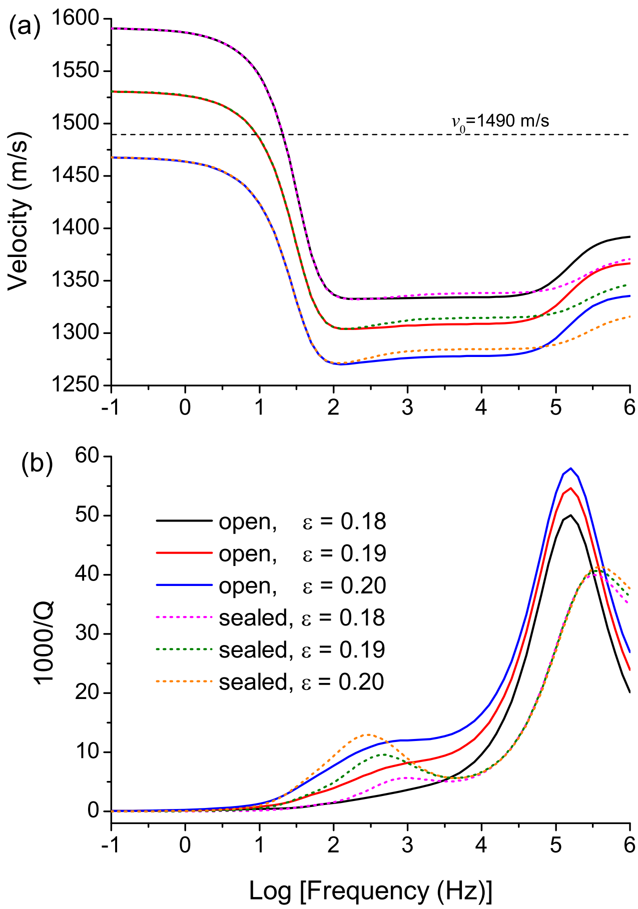

Figure 24. Effect of crack density ϵ on velocity dispersion (a) and dissipation factor (b) of the fundamental mode with $H = 10$ m. A constant $\gamma = 0.002$ is used. The LFF is present. The black dashed line corresponds to the velocity of the acoustic wave in water.

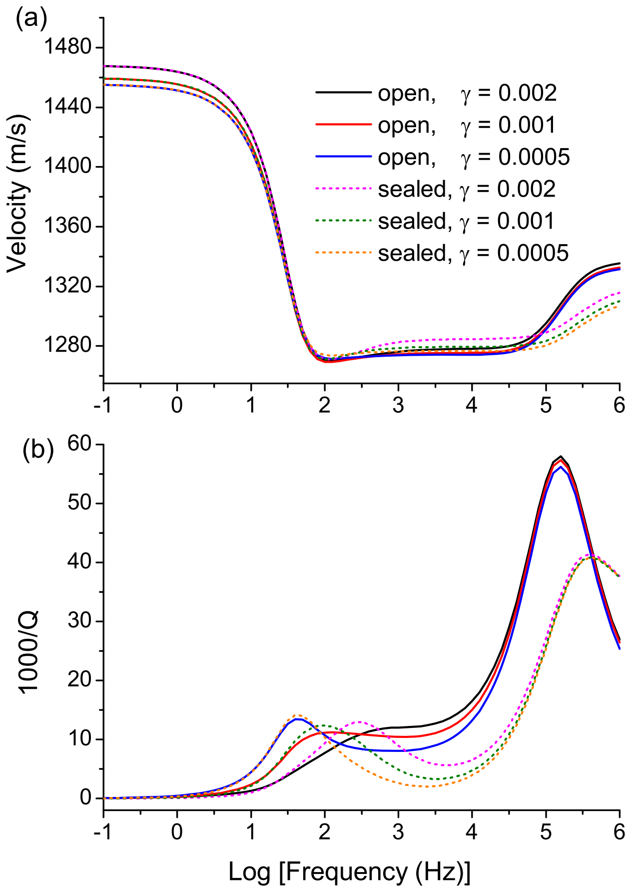

Figure 25. Effect of crack aspect ratio γ on velocity dispersion (a) and dissipation factor (b) of the fundamental mode with $H = 10$ m. A constant $\epsilon = 0.20$ is used. The LFF is present.

at the cut-off frequency and decreases as the frequency increases, reaching a limit equal to 1490 m/s, the velocity of the acoustic wave in water. Therefore, the higher-order modes are pseudo-Rayleigh waves. Decreasing H implies an increased cut-off frequency for each mode. Fig. 21 shows the phase velocity and dissipation factor of the first-order mode for two values of H. The presence of the LFF induces a higher attenuation at low frequencies, but the loss is quite small. It should be noted that, if the acoustic velocity in water is greater than the P1-wave velocity in the porous half-space, such higher-order surface modes do not exist.

Fig. 22 shows the displacements of the fundamental mode as a function of depth at 300 Hz for $H = 5$ m and 20 m, corresponding to 1.2 and 4.7 times the fundamental-mode wavelength, respectively. The variations are quite similar as those of Fig. 14. The fundamental mode loses its energy as the distance from the interface $z = 0$ increases. The displacements are not completely zero at the water surface when $z = -H = -5$ m, while they are zero when $H =$ 20 m. There is also a sharp variation in the horizontal displacement in porous medium, similarly indicating the change in trajectories of the particle motions. The ellipticity (HZ ratio) of the fundamental mode as a function of frequency at $z = 0$ is displayed in Fig. 23. At low frequencies, the ellipticity is much higher than that displayed in Fig. 15, and decreases as the frequency increases, in correspondence to the significant velocity dispersion when $H = 20$ m (see Figs 18 and 19). At high frequencies, the results become the same as those in Fig. 15. The effects of the LFF and BCs are similarly observed.

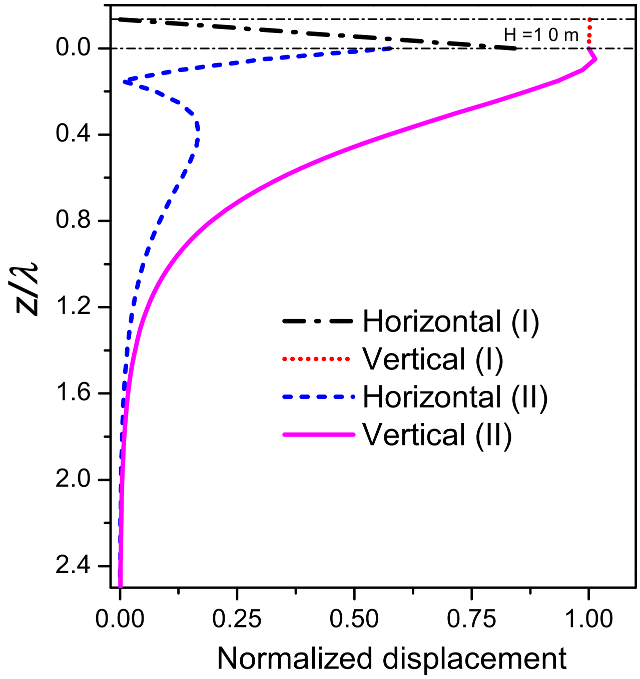

Figure 26. Absolute values of displacements of the fundamental mode (the pseudo-Rayleigh) as a function of depth at 20 Hz for $H = 10$ m. The displacements are normalized by the absolute vertical u_z at the surface ($z = 0$) in the double-porosity medium, and the depth is normalized by the pseudo-Rayleigh wavelength λ. The open-pore BCs are used and the LFF is present ($\epsilon = 0.18$, $\gamma = 0.002$).

Finally, Figs 24 and 25 show the effects of the crack density ϵ and aspect ratio γ on velocity and dissipation of the fundamental mode when $H = 10$ m. The effects are quite similar to those displayed in Figs 16 and 17, except that at low frequencies, a significant velocity dispersion (decrease) between 1 and 100 Hz is observed. Note that when $\epsilon = 0.18$ and 0.19, the velocities at low frequencies are higher than the fluid velocity (see Fig. 24a), because the asymptotic values at the low-frequency limit, equal to the velocity of the pseudo-Rayleigh wave, become larger than v_0, as shown in Fig. 9. This implies that in these cases the fundamental mode becomes the pseudo-Rayleigh wave that oscillates in the water layer. Fig. 26 shows the corresponding absolute pseudo-Rayleigh displacements as a function of depth for $\epsilon = 0.18$ and $\gamma = 0.002$, at a frequency of 20 Hz, where the phase velocity is 1494 m/s. In the water layer, the horizontal displacement decays to zero sharply, whereas the vertical one is not evidently attenuated, unlike the behavior of the pseudo-Stoneley wave in Fig. 22.

6 CONCLUSIONS

We have analyzed the propagation of surface waves at an interface between a water layer and a double-porosity half-space containing penny-shaped cracks, where local fluid flow (LFF) attenuation is present. Special cases are discussed by assuming the thickness of the water layer to be zero and infinity. In particular, we study the effects of the LFF, (open and sealed) boundary conditions (BCs) and crack density/aspect ratio on the surface-wave propagation. In the cases we study, we find a pseudo-Rayleigh wave for zero thickness, a pseudo-Stoneley wave for infinite thickness, and high-order surface modes for finite (non-zero) thickness. The results reveal the velocity dispersion and attenuation of all these waves. The LFF mechanism affects the propagation at frequencies less than 1 kHz, enhancing the attenuation, whereas the effects of the BCs are mainly observed at high frequencies. The crack density mainly affects the amount of mesoscopic attenuation, whereas the aspect ratio the location of the relaxation peak in the frequency band. The pseudo-Rayleigh wave propagates faster than the pseudo-Stoneley wave, with their respective dimensionless velocities relative to the shear wave being approximately 0.93 and 0.80. The fundamental mode exhibits a significant velocity dispersion, which moves to low frequencies when the thickness increases. In all cases, we additionally find two slower surface modes that resemble the slow P2 and P3 waves but exist only for sealed BCs, which are hardly affected by the LFF, BCs or the thickness of water layer. Future research includes the analysis of different medium properties and the derivation of analytical solutions based on the Green function.

ACKNOWLEDGMENTS

This work has been supported by the "National Nature Science Foundation of China (42174148, 41804095)", the "China Postdoctoral Science Foundation (2020M682242)", and the Postdoctoral Applied Research Project of Qingdao. We thank the Editors Ludovic Métivier and Louise Alexander, and the three reviewers for their helpful comments, which improve the quality of the paper significantly.

DATA AVAILABILITY

Data and codes can be available by contacting the corresponding author.

REFERENCES

Adler, L. & Nagy, P. B., 1994. Measurements of acoustic surface waves on fluid-filled porous rocks, *J. Geophys. Res.-Solid Earth,* **99**(B9), 17863–17869.

Ba, J., Carcione, J. M. & Nie, J., 2011. Biot-Rayleigh theory of wave propagation in double-porosity media, *J. Geophys. Res.-Solid Earth,* **116,** B06202, doi:10.1029/2010JB008185.

Biot, M. A., 1956. Theory of propagation of elastic waves in a fluid-saturated porous solid. I. Low frequency range, *J. Acoust. Soc. Am.,* **28**(2), 168–178.

Biot, M. A., 1962. Mechanics of deformation and acoustic propagation in porous media, *J. Appl. Phys.,* **33**(4), 1482–1498.

Budiansky, B. & O'connell, R. J., 1976. Elastic moduli of a cracked solid, *Int. J. Solids Struct.,* **12**(2), 81–97.

Carcione, J. M., 2022. *Wave Fields in Real Media. Theory and Numerical Simulation of Wave Propagation in Anisotropic, Anelastic, Porous and Electromagnetic Media,* Elsevier, Amsterdam, (4th edn, extended and revised).

Carcione, J. M., Gei, D., Gurevich, B. & Ba, J., 2021. On the normal-incidence reflection coefficient in porous media, *Surv. Geophys.,* **42**(4), 923–942.

Carcione, J. M. & Gurevich, B., 2011. Differential form and numerical implementation of Biot's poroelasticity equations with squirt dissipation, *Geophysics,* **76**(6), N55–N64.

Carcione, J.M., Morency, C. & Santos, J.E., 2010. Computational poroelasticity – a review, *Geophysics,* **75,** A229–A243.

Chao, G., Smeulders, D. M. J. & Van Dongen, M. E. H., 2006. Dispersive surface waves along partially saturated porous media, *J. Acoust. Soc. Am.,* **119**(3), 1347–1355.

Chapman, M., Zatsepin, S. V. & Crampin, S., 2002. Derivation of a microstructural poroelastic model, *Geophys. J. Int.,* **151**(2), 427–451.

Dai, Z. J., Kuang, Z. B. & Zhao, S. X., 2006. Rayleigh waves in a double porosity half-space, *J. Sound Vibrat.,* **298**(1–2), 319–332.

Deresiewicz, H., 1962. The effect of boundaries on wave propagation in a liquid-filled porous solid: IV. Surface waves in a half-space, *Bull. Seism. Soc. Am.,* **52**(3), 627–638.

Deresiewicz, H., 1964. The effect of boundaries on wave propagation in a liquid-filled porous solid: VII. Surface waves in a half-space in the presence of a liquid layer, *Bull. Seism. Soc. Am.,* **54**(1), 425–430.

Deresiewicz, H. & Skalak, R., 1963. On uniqueness in dynamic poroelasticity, *Bull. Seism. Soc. Am.,* **53**(4), 783–788.

Dvorkin, J., Mavko, G. & Nur, A., 1995. Squirt flow in fully saturated rocks, *Geophysics,* **60**(1), 97–107.

Dvorkin, J. & Nur, A., 1993. Dynamic poroelasticity: A unified model with the squirt and the Biot mechanisms, *Geophysics,* **58**(4), 524–533.

Feng, S. & Johnson, D. L., 1983. High-frequency acoustic properties of a fluid/porous solid interface. I. New surface mode, *J. Acoust. Soc. Am.,* **74**(3), 906–914.

Fu, B., Guo, J., Fu, L. Y., Glubokovskikh, S., Galvin, R. J. & Gurevich, B., 2018. Seismic dispersion and attenuation in saturated porous rock with aligned slit cracks, *J. Geophys. Res. Solid Earth,* **123**(8), 6890–6910.

Galvin, R. J. & Gurevich, B., 2009. Effective properties of a poroelastic medium containing a distribution of aligned cracks, *J. Geophys. Res. Solid Earth,* **114**(B7), doi:10.1029/2008JB006032.

Gubaidullin, A. A., Kuchugurina, O. Y., Smeulders, D. M. J. & Wisse, C. J., 2004. Frequency-dependent acoustic properties of a fluid/porous solid interface, *J. Acoust. Soc. Am.,* **116**(3), 1474–1480.

Guo, J. & Gurevich, B., 2020. Frequency-dependent P-wave anisotropy due to wave-induced fluid flow and elastic scattering in a fluid-saturated porous medium with aligned fractures, *J. Geophys. Res. Solid Earth,* **125**(8), e2020JB020320, doi:10.1029/2020JB020320.

Gurevich, B., Ciz, R. & Denneman, A. I., 2004. Simple expressions for normal-incidence reflection coefficients from an interface between fluid-saturated porous materials, *Geophysics,* **69**(6), 1372–1377.

Jakobsen, M. & Chapman, M., 2009. Unified theory of global flow and squirt flow in cracked porous media, *Geophysics,* **74**(2), WA65–WA76.

Kumari, M. & Kumar, M., 2022. Reflection of inhomogeneous waves at the surface of a cracked porous solid with penny-shaped inclusions, *Waves Random Complex Media,* **32**(4), 1992–2013.

Markov, M. G., 2009. Low-frequency Stoneley wave propagation at the interface of two porous half-spaces, *Geophys. J. Int.,* **177**(2), 603–608.

Mayes, M. J., Nagy, P. B., Adler, L., Bonner, B. P. & Streit, R., 1986. Excitation of surface waves of different modes at fluid-porous solid interface, *J. Acoust. Soc. Am.,* **79**(2), 249–252.

Muller, D. E., 1956. A method for solving algebraic equations using an automatic computer, *Math. Tables Other Aids Comput.,* **10**(56), 208–215.

Müller, T. M., Gurevich, B. & Lebedev, M., 2010. Seismic wave attenuation and dispersion resulting from wave-induced flow in porous rocks-a review, *Geophysics,* **75**(5), 75A147–75A164.

Nagy, P. B. & Blaho, G., 1994. Experimental measurements of surface stiffness on water-saturated porous solids, *The J. acoust. Soc. Am.,* **95**(2), 828–835.

Norris, A. N., 1989. Stoneley-wave attenuation and dispersion in permeable formations, *Geophysics,* **54**(3), 330–341.

Pride, S. R. & Berryman, J. G., 2003a. Linear dynamics of double porosity dual-permeability materials. I. Governing equations and acoustic attenuation, *Phys. Rev. E,* **68**(3), 036603, doi:10.1103/PhysRevE.68.036603.

Pride, S. R. & Berryman, J. G., 2003b. Linear dynamics of double porosity dual-permeability materials. II. Fluid transport equations, *Phys. Rev. E,* **68**(3), 036604, doi:10.1103/PhysRevE.68.036604.

Pride, S. R., Berryman, J. G. & Harris, J. M., 2004. Seismic attenuation due to wave-induced flow, *J. Geophys. Res. Solid Earth,* **109**(B1), doi:10.1029/2003JB002639.

Qi, Q., Cao, J., Wang, X. & Gao, J., 2021. Influence of interface condition on reflection of elastic waves in fluid-saturated porous media, *Geophysics,* **86**(4), MR223–MR233.

Qiu, H., Xia, T., Chen, W. & Yu, B., 2019. Low-frequency pseudo-Rayleigh and pseudo-Scholte waves at an interface of liquid/soft porous sediment with underlying hard porous sediment substrate, *Geophys. J. Int.,* **219**(1), 540–552.

Sharma, M. D., 1996. Surface-wave propagation in a cracked poroelastic half-space lying under a uniform layer of fluid, *Geophys. J. Int.,* **127**(1), 31–39.

Sharma, M. D., 2014. Effect of local fluid flow on Rayleigh waves in a double porosity solid, *Bull. Seism. Soc. Am.,* **104**(6), 2633–2643.

Sharma, M. D., 2018. Squirt-flow in fluid-saturated porous media: propagation of Rayleigh waves, *Transport Porous Media,* **122**(1), 25–42.

Sidler, R., Carcione, J. M. & Holliger, K., 2010. Simulation of surface waves in porous media, *Geophys. J. Int.,* **183**(2), 820–832.

Tajuddin, M., 1984. Rayleigh waves in a poroelastic half-space, *J. Acoust. Soc. Am.,* **75**(3), 682–684.

Tang, X., Chen, X. & Xu, X., 2012. A cracked porous medium elastic wave theory and its application to interpreting acoustic data from tight formations, *Geophysics,* **77**(6), D245–D252.

Tang, X. & Cheng, C. H., 1996. Fast inversion of formation permeability from Stoneley wave logs using a simplified Biot-Rosenbaum model, *Geophysics,* **61**(3), 639–645.

Thomsen, L., 1985. Biot-consistent elastic moduli of porous rocks: low-frequency limit, *Geophysics,* **50**(12), 2797–2807.

van Dalen, K. N., Drijkoningen, G. G. & Smeulders, D. M. J., 2011. Pseudo interface waves observed at the fluid/porous-medium interface. A comparison of two methods, *J. acoust. Soc. Am.,* **129**(5), 2912–2922.

Yang, J., 2005. Rayleigh surface waves in an idealised partially saturated soil, *Geotechnique,* **55**(5), 409–414.

Zhang, L., Ba, J., Carcione, J. M. & Sun, W., 2019. Modeling wave propagation in cracked porous media with penny-shaped inclusions, *Geophysics,* **84**(4), WA141–WA151.

Zhang, X. & Müller, T. M., 2019. Stoneley wave attenuation and dispersion and the dynamic permeability correction, *Geophysics,* **84**(4), WA1–WA10.

Zhang, Y., Xu, Y. & Xia, J., 2011. Analysis of dispersion and attenuation of surface waves in poroelastic media in the exploration-seismic frequency band, *Geophys. J. Int.,* **187**(2), 871–888.

APPENDIX A: EXPRESSIONS OF THE STIFFNESS AND DENSITY COEFFICIENTS

Following Zhang *et al.* (2019), the stiffness coefficients in eq. (7) are

$$\begin{aligned}
\lambda_c &= (1-\phi)K_s - \frac{2}{3}\mu_b + \left(2 - \frac{K_s}{K_f}\right)(\phi_1\alpha_1 M_1 + \phi_2\alpha_2 M_2) \\
&\quad - \left(1 - \frac{K_s}{K_f}\right)(\phi_1^2 M_1 + \phi_2^2 M_2), \\
\alpha_1 &= \frac{\beta\phi_1 K_s}{\gamma K_f} + \phi_1, \quad \alpha_2 = \frac{\phi_2 K_s}{\gamma K_f} + \phi_2, \\
M_1 &= \frac{K_f}{(\beta/\gamma+1)\phi_1}, \quad M_2 = \frac{K_f}{(1/\gamma+1)\phi_2}, \\
\gamma &= \frac{K_s}{K_f}\left[\frac{\beta\phi_1+\phi_2}{1-\phi-K_b/K_s}\right], \quad \beta = \frac{\phi_{20}}{\phi_{10}}\left[\frac{1-(1-\phi_{10})K_s/K_{b1}}{1-(1-\phi_{20})K_s/K_{b2}}\right],
\end{aligned} \tag{A1}$$

where $\phi = \phi_1 + \phi_2$ is the total porosity, K_s and K_f are the bulk moduli of the solid and fluid, K_b is the dry-rock modulus, which should be Biot-consistent (Thomsen 1985):

$$K_b = \frac{2}{3}\frac{1+\upsilon_B}{1-2\upsilon_B}\mu_b, \tag{A2}$$

with

$$\begin{aligned}
\mu_b &= \mu_s\left(1 - \frac{\phi_1}{1-b_B} - B_B\varepsilon\right), \\
b_B &= \frac{2}{15}\frac{4-5\upsilon_B}{1-\upsilon_B}, \quad B_B = \frac{32}{45}\frac{(1-\upsilon_B)(5-\upsilon_B)}{2-\upsilon_B},
\end{aligned} \tag{A3}$$

where μ_s is the grain shear modulus, υ_B is the Poisson ratio, and ε is the crack density; K_{b1} and K_{b2} are the dry-rock bulk moduli of the host medium and inclusions, which can be determined from

$$K_{b1} = \frac{(1-\phi_{10})K_s}{1+c_1\phi_{10}}, \quad \frac{f_2}{K_{b2}} = \frac{1}{K_b} - \frac{f_1}{K_{b1}}, \tag{A4}$$

where c_1 is the consolidation parameter of the host medium.

In the uniform-porosity case, the corresponding quantities in eq. (2) are

$$\begin{aligned}
&A = (1-\phi)K_s - 2N/3 - K_s(Q_1+Q_2)/K_f, \quad N = \mu_b, \\
&Q_1 = \alpha_1 M_1\phi_1 - M_1\phi_1^2, \quad R_1 = M_1\phi_1^2, \\
&Q_2 = \alpha_2 M_2\phi_2 - M_2\phi_2^2, \quad R_2 = M_2\phi_2^2.
\end{aligned} \tag{A5}$$

The five density coefficients ρ_{ij} in eq. (4), defined in the same manner as Biot (1962), are

$$\begin{aligned}
&\rho_{00} = (1-\phi)\rho_s - \rho_f(\phi-1)/2, \\
&\rho_{11} = (\phi_1+f_1)\rho_f/2, \quad \rho_{22} = (\phi_2+f_2)\rho_f/2, \\
&\rho_{01} = (\phi_1-f_1)\rho_f/2, \quad \rho_{02} = (\phi_2-f_2)\rho_f/2,
\end{aligned} \tag{A6}$$

where ρ_s is the grain density.

APPENDIX B: COMPONENTS OF M IN EQ. (29)

Defining

$$\begin{aligned}
n_1 &= \lambda_c - \alpha_1 M_1\phi_1 - \alpha_2 M_2\phi_2 + d_1(\alpha_1 M_1\phi_1\phi_2 - \alpha_2 M_2\phi_1\phi_2), \\
n_2 &= \alpha_1 M_1\phi_1 + d_2(\alpha_1 M_1\phi_1\phi_2 - \alpha_2 M_2\phi_1\phi_2), \\
n_3 &= \alpha_2 M_2\phi_2 + d_3(\alpha_1 M_1\phi_1\phi_2 - \alpha_2 M_2\phi_1\phi_2), \\
h_1 &= -\alpha_1 M_1 + M_1\phi_1 - M_1\phi_1\phi_2 d_1, \\
h_2 &= -M_1\phi_1 - M_1\phi_1\phi_2 d_2, \\
h_3 &= -M_1\phi_1\phi_2 d_3, \\
g_1 &= -\alpha_2 M_2 + M_2\phi_2 + M_2\phi_1\phi_2 d_1, \\
g_2 &= M_2\phi_1\phi_2 d_2, \\
g_3 &= -M_2\phi_2 + M_2\phi_1\phi_2 d_3,
\end{aligned} \tag{B1}$$

the elements of matrix **M** are

$$\begin{aligned}
&M_{00} = 0, \quad M_{01} = 2\xi_1, \quad M_{02} = 2\xi_2, \quad M_{03} = 2\xi_3, \\
&M_{04} = -\mathrm{i}(1+\xi_4^2),
\end{aligned} \tag{B2}$$

$$\begin{aligned}
M_{10} &= -(1-\exp[-2kH\xi_0])\rho_0, \\
M_{11} &= (n_1 + n_2\nu_1 + n_3\delta_1 + 2\mu_b)(1/v_1^2) - 2\mu_b/c^2, \\
M_{12} &= (n_1 + n_2\nu_2 + n_3\delta_2 + 2\mu_b)(1/v_2^2) - 2\mu_b/c^2, \\
M_{13} &= (n_1 + n_2\nu_3 + n_3\delta_3 + 2\mu_b)(1/v_3^2) - 2\mu_b/c^2, \\
M_{14} &= 2\mathrm{i}\mu_b\xi_4/c^2,
\end{aligned} \tag{B3}$$

$$\begin{aligned}
M_{20} &= \xi_0(1+\exp[-2kH\xi_0]), \\
M_{21} &= \xi_1(1-\phi_1-\phi_2+\phi_1\nu_1+\phi_2\delta_1), \\
M_{22} &= \xi_2(1-\phi_1-\phi_2+\phi_1\nu_2+\phi_2\delta_2), \\
M_{23} &= \xi_3(1-\phi_1-\phi_2+\phi_1\nu_3+\phi_2\delta_3), \\
M_{24} &= -\mathrm{i}(1-\phi_1-\phi_2+\phi_1\nu_4+\phi_2\delta_4),
\end{aligned} \tag{B4}$$

$$M_{30} = -(1-\exp[-2kH\xi_0])\rho_0,$$
$$M_{31} = -(h_1+h_2\nu_1+h_3\delta_1)/v_1^2 + \mathrm{i}(\nu_1-1)\sqrt{\frac{1}{c^2}-\frac{1}{v_1^2}}Z_1\phi_1,$$
$$M_{32} = -(h_1+h_2\nu_2+h_3\delta_2)/v_2^2 + \mathrm{i}(\nu_2-1)\sqrt{\frac{1}{c^2}-\frac{1}{v_2^2}}Z_1\phi_1,$$
$$M_{33} = -(h_1+h_2\nu_3+h_3\delta_3)/v_3^2 + \mathrm{i}(\nu_3-1)\sqrt{\frac{1}{c^2}-\frac{1}{v_3^2}}Z_1\phi_1,$$
$$M_{34} = (\nu_4-1)\frac{1}{c}Z_1\phi_1, \tag{B5}$$
$$M_{40} = -(1-\exp[-2kH\xi_0])\rho_0,$$
$$M_{41} = -(g_1+g_2\nu_1+g_3\delta_1)/v_1^2 + \mathrm{i}(\delta_1-1)\sqrt{\frac{1}{c^2}-\frac{1}{v_1^2}}Z_2\phi_2,$$
$$M_{42} = -(g_1+g_2\nu_2+g_3\delta_2)/v_2^2 + \mathrm{i}(\delta_2-1)\sqrt{\frac{1}{c^2}-\frac{1}{v_2^2}}Z_2\phi_2,$$
$$M_{43} = -(g_1+g_2\nu_3+g_3\delta_3)/v_3^2 + \mathrm{i}(\delta_3-1)\sqrt{\frac{1}{c^2}-\frac{1}{v_3^2}}Z_2\phi_2,$$
$$M_{44} = (\delta_4-1)\frac{1}{c}Z_2\phi_2. \tag{B6}$$

APPENDIX C: BIOT AND FENG AND JOHNSON EQUATIONS AS A PARTICULAR CASE

We show that the double-porosity model reduces to the Biot theory when some quantities are zero, and the corresponding equations derived from the BCs become those of Feng & Johnson (1983) at a fluid/porous-medium interface.

Considering $\phi_{20} = f_2 = 0$, as given in Appendix A, $Q_2 = R_2 = 0$. Correspondingly, ς does not play a role. Then, eq. (2) becomes

$$\begin{aligned}\sigma_1 &= -\phi_1 P_{f1} = Q_1\epsilon + R_1\eta^{(1)},\\ \sigma_{ij} &= 2N\epsilon_{ij} + \left[A\epsilon + Q_1\eta^{(1)}\right]\delta_{ij}.\end{aligned} \tag{C1}$$

Also, $b_2 = 0$, and $\rho_{22} = \rho_{02} = 0$, and eq. (4) reduces to

$$\begin{aligned}\sigma_{ij,j} &= \rho_{00}\ddot{u}_i + \rho_{01}\ddot{U}_i^{(1)} + b_1(\dot{u}_i - \dot{U}_i^{(1)}),\\ (\sigma_1)_{,i} &= \rho_{01}\ddot{u}_i + \rho_{11}\ddot{U}_i^{(1)} - b_1(\dot{u}_i - \dot{U}_i^{(1)}).\end{aligned} \tag{C2}$$

Then, eqs (5) becomes the classic Biot theory (1962):

$$\begin{aligned}&N\nabla^2\mathbf{u} + (A+N)\nabla\epsilon + Q_1\nabla\eta^{(1)} = \rho_{00}\ddot{\mathbf{u}} + \rho_{01}\ddot{\mathbf{U}}^{(1)}\\ &\quad + b_1(\dot{\mathbf{u}} - \dot{\mathbf{U}}^{(1)}),\\ &Q_1\nabla\epsilon + R_1\nabla\eta^{(1)} = \rho_{01}\ddot{\mathbf{u}} + \rho_{11}\ddot{\mathbf{U}}^{(1)} - b_1(\dot{\mathbf{u}} - \dot{\mathbf{U}}^{(1)}).\end{aligned} \tag{C3}$$

Based on the Helmholtz decomposition, we similarly have

$$\mathbf{u} = \nabla\varphi_0 + \nabla\times\mathbf{\Psi_0}, \quad \mathbf{U}^{(1)} = \nabla\varphi_1 + \nabla\times\mathbf{\Psi_1}, \tag{C4}$$

with

$$\begin{cases}\varphi_0 = A_0\exp\left[\mathrm{i}(\mathbf{k_p}\cdot\mathbf{r} - \omega t)\right]\\ \varphi_1 = A_1\exp\left[\mathrm{i}(\mathbf{k_p}\cdot\mathbf{r} - \omega t)\right]\end{cases}, \quad \begin{cases}\Psi_0 = B_0\exp\left[\mathrm{i}(\mathbf{k_s}\cdot\mathbf{r} - \omega t)\right]\\ \Psi_1 = B_1\exp\left[\mathrm{i}(\mathbf{k_s}\cdot\mathbf{r} - \omega t)\right]\end{cases}. \tag{C5}$$

Applying the divergence operator to eq. (C3), we have

$$\mathbf{Y}\cdot\mathbf{A} = \mathbf{0}, \tag{C6}$$

where $\mathbf{A} = [A_0, A_1]^{\mathrm{T}}$, and the components of $\mathbf{Y}$ are

$$\begin{cases}Y_{11} = (A+2N)k_p^2 - \rho_{00}\omega^2 - \mathrm{i}\omega b_1,\\ Y_{12} = Y_{21} = Q_1 k_p^2 - \rho_{01}\omega^2 + \mathrm{i}\omega b_1,\\ Y_{22} = R_1 k_p^2 - \rho_{11}\omega^2 - \mathrm{i}\omega b_1,\end{cases} \tag{C7}$$

which gives two complex roots (k_1 and k_2), corresponding to the fast P1 and slow P2 waves, respectively. Solving eq. (C6), we obtain the amplitude ratio $\frac{A_1}{A_0}$ at the specific k_i as

$$\frac{A_1}{A_0}|_{k=k_i} = -\frac{Y_{11}}{Y_{12}}|_{k=k_i} = \nu_i. \tag{C8}$$

Those two ratios (ν_1 and ν_2) correspond to $-G_+$ and $-G_-$ in Feng & Johnson (1983), respectively.

Similarly, for the shear wave, we have

$$\mathbf{E}\cdot\mathbf{B} = \mathbf{0}, \tag{C9}$$

where, $\mathbf{B} = [B_0, B_1]^{\mathrm{T}}$, and the components of $\mathbf{E}$ are

$$\begin{cases}E_{11} = Nk_s^2 - \rho_{00}\omega^2 - \mathrm{i}\omega b_1,\\ E_{12} = E_{21} = -\rho_{01}\omega^2 + \mathrm{i}\omega b_1,\\ E_{22} = -\rho_{11}\omega^2 - \mathrm{i}\omega b_1.\end{cases} \tag{C10}$$

There exists one complex root (k_3), and the amplitude ratio becomes

$$\frac{B_1}{B_0} = -\frac{E_{21}}{E_{22}} = \nu_4, \tag{C11}$$

which corresponds to $\frac{\tilde{\alpha}-1}{\tilde{\alpha}}$ in eq. (A5) of Feng & Johnson (1983).

In the Biot medium ($z > 0$), the displacements of the solid and fluid particles are

$$u_x = \sum_{j=1}^{2}\frac{\partial\Phi_j}{\partial x} - \frac{\partial\Phi_4}{\partial z}, \qquad u_z = \sum_{j=1}^{2}\frac{\partial\Phi_j}{\partial z} + \frac{\partial\Phi_4}{\partial x},$$
$$U_x^{(1)} = \sum_{j=1}^{2}\nu_j\frac{\partial\Phi_j}{\partial x} - \nu_4\frac{\partial\Phi_4}{\partial z}, \quad U_z^{(1)} = \sum_{j=1}^{2}\nu_j\frac{\partial\Phi_j}{\partial z} + \nu_4\frac{\partial\Phi_4}{\partial x}, \tag{C12}$$

where Φ_1, Φ_2 and Φ_4 correspond to the P1, P2 and SV waves, which can be expressed as in eq. (24).

At the interface, the following BCs are satisfied as

$$\begin{aligned}&(\sigma_{xz})_{\mathrm{II}} = 0,\\ &(\tau_{zz})_{\mathrm{I}} = (\sigma_{zz})_{\mathrm{II}} + (\sigma_1)_{\mathrm{II}},\\ &(u_z)_{\mathrm{I}} = (u_z)_{\mathrm{II}} + \phi_1(U_z^{(1)} - u_z)_{\mathrm{II}},\\ &(p_f)_{\mathrm{I}} - (P_{f1})_{\mathrm{II}} = Z_1\phi_1(\dot{U}_z^{(1)} - \dot{u}_z)_{\mathrm{II}}.\end{aligned} \tag{C13}$$

These BCs form a system of equations of order four as follows

$$\mathbf{ND^b} = \mathbf{0}, \tag{C14}$$

where $\mathbf{D^b} = [D_0, D_1, D_2, D_4]^T$, and the elements of $\mathbf{N}$ are

$$N_{00} = 0, \; N_{01} = 2\xi_1, \; N_{02} = 2\xi_2, \; N_{03} = -\mathrm{i}(1+\xi_{4^2}), \tag{C15}$$

$$\begin{aligned}&N_{10} = -(1-\exp[-2kH\xi_0])\rho_0,\\ &N_{11} = (A+Q_1+\nu_1(R_1+Q_1)+2N)(1/v_1^2) - 2N/c^2,\\ &N_{12} = (A+Q_1+\nu_2(R_1+Q_1)+2N)(1/v_2^2) - 2N/c^2,\\ &N_{13} = 2\mathrm{i}N\xi_4/c^2,\end{aligned} \tag{C16}$$

$$N_{20} = \xi_0(1+\exp[-2kH\xi_0]),$$
$$N_{21} = \xi_1(1-\phi_1+\phi_1\nu_1),$$
$$N_{22} = \xi_2(1-\phi_1+\phi_1\nu_2),$$
$$N_{23} = -\mathrm{i}(1-\phi_1+\phi_1\nu_4), \quad \text{(C17)}$$

$$N_{30} = -(1-\exp[-2kH\xi_0])\rho_0,$$
$$N_{31} = (Q_1+R_1\nu_1)/\phi_1/v_1^2 + \mathrm{i}(\nu_1-1)\sqrt{\frac{1}{c^2}-\frac{1}{v_1^2}}Z_1\phi_1,$$
$$N_{32} = (Q_1+R_1\nu_2)/\phi_1/v_2^2 + \mathrm{i}(\nu_2-1)\sqrt{\frac{1}{c^2}-\frac{1}{v_2^2}}Z_1\phi_1,$$
$$N_{33} = (\nu_4-1)\frac{1}{c}Z_1\phi_1. \quad \text{(C18)}$$

It is evident that the above equation can be derived by letting $\phi_2 = 0$ in the elements of **M** and then eliminating the fourth column and fifth row.

Now, we compare eqs (C14) with those of Feng & Johnson (1983). By letting $H = +\infty$, and $P = A + 2N$, and defining

$$D_0 = C_0,\quad D_1 = C_1,\quad D_2 = C_2,\quad D_4 = iC_4$$
$$\nu_1 = -G_+,\quad \nu_2 = -G_-,\quad \nu_4 = \frac{\tilde{\alpha}-1}{\tilde{\alpha}},\quad Z_1 = T, \quad \text{(C19)}$$

in the same manner as Feng & Johnson (1983), the first equation in (C14) becomes

$$2\xi_1 C_1 + 2\xi_2 C_2 + (1+\xi_4^2)C_4 = 0. \quad \text{(C20)}$$

After a simplification, we derive eq. (C2) of Feng & Johnson (1983).

The second equation in (C14) becomes

$$\rho_0 c^2 C_0 + \left(\frac{[G_+(R_1+Q_1)-(P+Q_1)]\,c^2}{v_1^2}+2N\right)C_1$$
$$+ \left(\frac{[G_-(R_1+Q_1)-(P+Q_1)]\,c^2}{v_2^2}+2N\right)C_2$$
$$+\ 2N\xi_4 C_4 = 0, \quad \text{(C21)}$$

which is eq. (C1) of Feng & Johnson (1983).

The third equation in (C14) becomes

$$\xi_0 C_0 + \xi_1(1-\phi_1-\phi_1 G_+)C_1 + \xi_2(1-\phi_1-\phi_1 G_-)C_2$$
$$+\left(1-\frac{\phi_1}{\tilde{\alpha}}\right)C_4 = 0, \quad \text{(C22)}$$

which is eq. (C3) of Feng & Johnson (1983).

The last equation in (C14) becomes

$$-\rho_0 C_0 + \left[\frac{Q_1-R_1G_+}{\phi_1 v_1^2} - \mathrm{i}\frac{(G_++1)\xi_1 T\phi_1}{c}\right]C_1$$
$$+\left[\frac{Q_1-R_1G_-}{\phi_1 v_2^2} - \mathrm{i}\frac{(G_-+1)\xi_2 T\phi_1}{c}\right]C_2 - \mathrm{i}\frac{T\phi_1}{c\tilde{\alpha}}C_4 = 0. \quad \text{(C23)}$$

By multiplying $-\phi_1 c^2$ on both sides, we derive eq. (C4) of Feng & Johnson (1983).